CZECH TECHNICAL UNIVERSITY IN PRAGUE

FACULTY OF ELECTRICAL ENGINEERING

DEPARTMENT OF ELECTROMAGNETICAL FIELD

DIPLOMA THESIS

# Design of 3D printed circularly polarized waveguide antenna

AUTHOR

# ADAM ROXER

SUPERVISOR

# DOC. ING. PAVEL HAZDRA, PH.D.

PRAGUE, MAY 27, 2016

## Anotace

Tato diplomová práce se zabývá inovovaným typem polarizátoru vestavěným ve vlnovodné struktuře. Tento polarizátor zajišťuje přeměnu lineárně polarizované vlny na kruhově polarizovanou vlnu. V programu CST Studio Suite jsou navrženy dva typy polarizátoru, jeden v kruhovém vlnovodu s podélnými destičkami po stranách a druhý v eliptickém vlnovodu. Oba polarizátory jsou následně vyrobeny tiskem na 3D tiskárně, pokoveny třemi různými technologiemi a jsou vybaveny SMA konektorem se sondou. Ve stíněné komoře je provedeno měření základních parametrů a naměřená data jsou porovnána s daty simulovanými.

## Klíčová slova

Polarizátor, kruhově polarizovaná anténa, kruhový vlnovod, eliptický vlnovod, 3D tiskárna, pokovení, osový poměr.

## Abstract

This diploma thesis deals with a novel type of polarizer in the waveguide structure. This polarizer transforms polarization of the wave from linear to circular. Using CST Studio Suite two polarizer are designed, one in the circular waveguide with perturbation plates at opposite sides and the second one in the elliptical waveguide. Both polarizers are manufactured by printing on a 3D printer, metallized with three different techniques and equipped with a SMA connector with an electrical probe. At the end a measurement is shown and the measured parameters are compared with the simulated parameters.

## Key Words

Polarizer, circularly polarized antenna, circular waveguide, elliptical waveguide, 3D printer, metallizing, axial ratio.

## Declaration

I hereby declare that I have completed this diploma thesis independently and that I have listed all the information sources used in compliance with the Metodical instruction about observing etical principles during preparation university final theses.

Prague, May 27, 2016

. . . . . . . . . . . . . . . . . . . . . . . . . . . . . . . .

Author signature

## Acknowledgments

I would like to thank to my supervisor, Doc. Ing. Pavel Hazdra, PhD., for his support and patient guidance and encouragement during this project. Special thanks belongs to Ing. Petr Dvořák, PhD. for his accommodating help with the 3D printer and to Ing. Václav Kabourek for his helpfulness with antenna measurement. I appreciate positive approach of the company Zlín Precision s.r.o., which performed the metallizing of the developed antenna. I would like to thank to my family and my girlfriend Denisa for their support during the whole studies.

## Čestné prohlášení

Prohlašuji, že jsem předloženou práci vypracoval samostatně a že jsem uvedl veškeré použité informační zdroje v souladu s Metodickým pokynem o dodržování etických principů při přípravě vysokoškolských závěrečných prací.

V Praze, 27. května 2016

. . . . . . . . . . . . . . . . . . . . . . . . . . . . . . . .

Podpis autora

# Contents

# List of used symbols

| | |
|---|---|
| $E$ | electric field |
| $B$ | magnetic field |
| $f_d$ | design frequency |
| $k$ | wavenumber |
| $V$ | Verdet constant |
| $\epsilon_0$ | vacuum permittivity |
| $\Gamma$ | reflection coefficient |
| $\lambda_g$ | guide wavelength |
| $\mu_0$ | vacuum permeability |
| $\omega$ | angular frequency |

# List of used abbreviations

| | |
|---|---|
| AR | Axial Ratio |
| BW | Bandwidth |
| FIT | Finite Integration Technique |
| HPBW | Half-Power Beamwidth |
| LHCP | Left-Hand Circular Polarization |
| PFL | Polarization Loss Factor |
| RFID | Radio Frequency Identification |
| RHCP | Right-Hand Circular Polarization |
| RL | Return Loss |
| TE | Tranvserse Electric |
| TM | Transvers Magnetic |
| TEM | Transverse Electromagnetic |
| VSWR | Voltage Standing Wave Ratio |

# 1 Introduction

Circular polarization and circularly polarized antennas are widely used in the satellite communication since they are suitable for reliable data transmission over a long way through the atmosphere. There are not many antennas working with the circular polarization naturally. Such polarizer have been typically proposed and developed using the septum or irises structure placed inside the waveguide structure. The manufacturing of such polarizers can be very complicated for common machining methods and the quality and accuracy can not be guaranteed. The main goal of this thesis is to design a circular polarizer arranged in the circular waveguide structure, which can be easily manufactured using a modern 3D printing technology and has a compact embodiment. Since the printer can not print electrical conductive materials, the polarizer needs to be layered with a metal layer. This polarizer will be measured and the measured data will be analysed and compared with the simulation. The design frequency $f_d$= 3 GHz will be considered to enable the 3D printing with limited dimensions.

# 2 Antennas

An antenna is a device for transformation of the electromagnetic wave travelling through the free space into the guided wave in the transmission line as in Fig. 1. The antenna can be thus used for receiving, but also for transmitting of the electromagnetic waves due to the reciprocity of the antennas, whereas the parameters, like radiating pattern or antenna gain are the same for both operating modes. In specific case and appropriate design involving two orthogonal polarizations, an antenna can serve both receiving and transmitting.
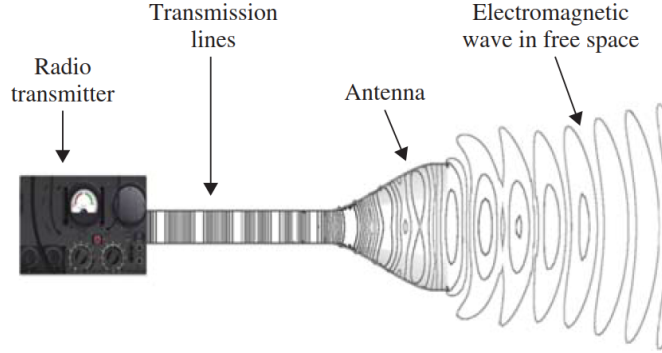


Figure 1: An antenna providing transformation from guided waves to free space waves, taken from [5].

## 2.1 Input impedance

The input impedance $Z_{in}$ is defined as an impedance of the antenna at its feeding terminals or as the ratio of the voltage and current at the terminals [8]. The input impedance is usually a complex number and can be expressed as

$$Z_{in} = R_r + R_{loss} + \mathrm{j}X_A \tag{1}$$

where $R_r$ is a radiation resistance of the antenna, $R_{loss}$ is a loss resistance of the antenna and $X_A$ is an antenna reactance.

The Fig. 2 shows a situation when the antenna is connected to the generator with internal impedance $Z_G = R_G + \mathrm{j}X_G$. For the matching of the antenna to the generator and delivering of the maximum power to the antenna, both impedance has to be conjugated, thus $Z_G = Z_A^*$. This condition is fulfilled for

$$R_G = R_r + R_{loss}$$

$$X_G = -X_A \tag{2}$$

## 2.2 Reflection coefficient

For the efficient transmission of the electromagnetic waves into the antenna, the input impedance $Z_{in}$ needs to be matched with the characteristic impedance of the feeding
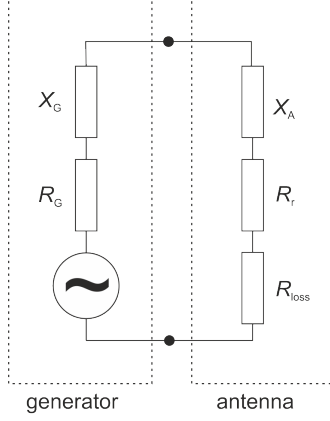
Figure 2: An alternative circuit schematic of the antenna.

transmission line. Usually 50 Ω cables are used in the radiofrequency applications, but also another values of impedance can be obtained, for example 75 Ω for television and satellite technique. For standard 50 Ω cables the antenna impedance should be equal to 50 Ω. In case these impedance are different a reflections at the transition occurs and part of the power is reflected back to the generator, what is not desired. The reflection coefficient gives a ratio of the reflected wave voltage to the incident voltage [8] and the definition with the impedances it is given by

$$\Gamma = \frac{Z_{in} - Z_0}{Z_{in} + Z_0} \tag{3}$$

where $Z_{in}$ is an input impedance of the antenna and $Z_0$ is the characteristic impedance of the transmission line used for the antenna feeding. In practise, usually another formulation is used, the return loss with dB units defined by

$$RL = -20 \log |\Gamma| \tag{4}$$

Well designed antennas have the return loss usually 10 dB and higher, e.g. the return loss of 20 dB corresponds to reflection of 1% of the input power. From the return loss a next parameter can derived, a voltage standing wave ratio (VSWR). VSWR represents the ratio of the maximum voltage $V_{\max}$ to the minimum voltage $V_{\min}$ on the transmission line and is given by

$$VSWR = \frac{|V_{\max}|}{|V_{\min}|} = \frac{1 + |\Gamma|}{1 - |\Gamma|} \tag{5}$$

The reflection coefficient can be also related to the reflected power $P_r$ and incoming power $P_i$ by

$$P_r = P_i \, |\Gamma|^2 \tag{6}$$

3

## 2.3 Directivity, gain, efficiency

The radiation property of the antenna to direct its power towards a given direction $(\theta, \phi)$, is defined with a directive gain, which describes the radiation intensity normalized to the intensity $U_i$ of the isotropic antenna with the same radiated power. The directive gain is defined [8] as

$$D(\theta, \phi) = \frac{U(\theta, \phi)}{U_i} = \frac{U(\theta, \phi)}{\frac{P_{rad}}{4\pi}} \tag{7}$$

The directivity $D_{max}$, or just $D$ is then defined as the directive gain in a direction to the maximal electric field intensity $U_{max}$

$$D_{max} = \frac{U_{max}}{U_i} \tag{8}$$

The gain of the antenna is derived from the directivity, but it includes the efficiency $\eta$, which is linked with the losses in the antenna

$$G(\theta, \phi) = \eta D(\theta, \phi) \tag{9}$$

The total efficiency $\eta$ can be divide in particular efficiencies as [8]

$$\eta = \eta_r \eta_c \eta_d \tag{10}$$

where $\eta_r$ is reflection efficiency being related to the reflections at the antenna input, $\eta_c$ is conduction efficiency related to the material of the antenna and $\eta_d$ is dielectric efficiency related to the presence of the dielectric material in the antenna.

For practical reasons both directivity and gain are usually expressed in dB, so that is $D_{dB} = 10 \log D$ and $G_{dB} = 10 \log G$. The gain of the antenna is usually used in dBi, what means the relation to an isotropic antenna. When referred to the dipole antenna, dBd unit are used. Because of the dipole antenna gain 2.15 dB, these mutual conversion can be given dBi= dBd+2.15 and dBd=dBi-2.15.

The beamwidth of the radiation pattern is an angular separation between two identical points to both sides of the maximum of the radiation pattern. Usually half-power band-width (HPBW) is used, which is determined by the angles where the power is half compared to the power in the maximum (-3 dB).

## 2.4 Bandwidth

A frequency bandwidth of the antenna is an frequency interval, where behaviours of the antenna satisfies certain requirement. The usual parameter for the antenna bandwidth is the minimal return loss and so the lower and upper frequencies are determined.

$$BW = \frac{f_2 - f_1}{f_0} \times 100 \tag{11}$$

where $f_1$ and $f_2$ are the lower and upper frequencies and $f_0$ is the central frequency.

For circularly polarized antenna, not only the impedance matching, described with the reflection coefficient, but also an bandwidth of the sufficient circular polarization, described with the the axial ratio, should be satisfied. The good circularly polarized antenna should have the axial ratio below 3 dB [5].

## 2.5 Field regions

The regions around the antenna can be subdivided into three regions according the distance from the antenna, as shown in Fig. 3. These regions are **reactive near field**, **radiating near field** and **far field**. Most of the antenna characteristics are defined and valid only in the far field region, where the field is fully transversal.
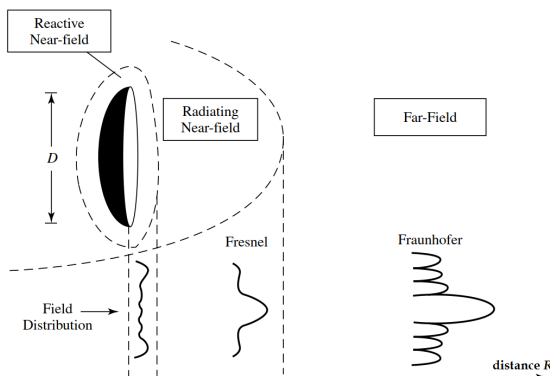


Figure 3: Radiation pattern in different antenna regions, taken from [8].

The first region nearest to the antenna is called a reactive near field. In this region a reactive field dominates, but the reactive components varies inversely with the $\frac{1}{R^3}$ and thus they disappear very quickly. The reactive near field region of the antenna with largest diameter $D$ (assumed $D > \lambda$) and the wavelength $\lambda$ is bounden by the distance $R$ from the antenna

$$R < 0.62\sqrt{\frac{D^3}{\lambda}} \tag{12}$$

The next region is called a radiative near field, also Fresnel region and it is a region where the field begins to radiate. The distance interval for the radiative near field is given by

$$0.62\sqrt{\frac{D^3}{\lambda}} < R < \frac{2D^2}{\lambda} \tag{13}$$

The furthest region of the antenna is the far field, also called Fraunhofer region, beginning in the distance

$$R > \frac{2D^2}{\lambda} \tag{14}$$

5

This distance is defined by the maximal phase error of $\frac{\phi}{8}$ and the most antenna characteristics, like radiating pattern or directivity, are valid only in the far field. The electromagnetic field is there transversal, the electric and magnetic fields are in phase with each other and thus the impedance of the far field is constant and given by

$$Z_0 = \sqrt{\frac{\mu_0}{\epsilon_0}} \qquad (15)$$

where $\mu_0$ is the vacuum permeability and $\epsilon_0$ the vacuum permittivity.

# 3 Polarization

The polarization in the electromagnetic theory is defined as the orientation of the electric field vector. This vector can oscillate in the fixed direction or can rotate with time. Hence, we can distinguish two general arrangement of the polarization- linear polarization and elliptical polarization with a special case of circular polarization. The desirable component of the wave, which has the desired sense of polarization (vertical or horizontal for linear polarization) or sense of rotation (RHCP or LHCP) for circular polarization, is called the **co-polarization** component. On the other hand, the undesirable component, i.e. vertical component for the horizontal antenna or RHCP component for the LHCP antenna, is called **cross-polarization** component.

## 3.1 Linear polarization

Linear polarization is a state of the electric field vector $E$, that does not change in the time, and directs in a fixed direction. We can distinguish vertical or horizontal polarization, whereas antenna is to be said vertically polarized when its electrical field is perpendicular to the Earth's surface and horizontal when its electric field is horizontal with the Earth's surface. The sense of polarization is given only by the antenna arrangement, so e.g. rotating a horizontal linear antenna at 90° we get vertical linear antenna arrangement. As described below, linear polarization can be described as a special case of the elliptical polarization.

For linear polarization of the electromagnetic wave travelling in the positive $z$ direction, we can write the electric field $E$ as

$$\vec{E} = E\hat{x}e^{-jk_0z} \tag{16}$$

Most of the transmitting systems use linear polarized antennas for easier manufacturing and less complexity when compared to the circular polarized systems. For example, systems like TV broadcasting in the Czech Republic used a linear polarization in the horizontal arrangement, today's DVB-T broadcasting use both vertical and horizontal linear polarization, Wi-Fi networks use commonly linear polarization or GSM mobile phone system use also a linear polarized antenna in the mobile phone, there the circularly polarized antenna would be demanding to be implemented in the mobile phones.

## 3.2 Elliptical polarization

When we consider a superposition of two linearly polarized waves $\hat{x}$ and $\hat{y}$ with amplitudes $E_1$ and $E_2$, which both travel in the positive $z$ direction, the total electric field can be written as [7]

$$\vec{E} = (E_1\hat{x} + E_2\hat{y})e^{-jk_0z} \tag{17}$$

There are more possibilities according to the size of electrical intensity $E_1$ and $E_2$. Special cases are if $E_1 = 0$ or $E_2 = 0$, the wave is then polarized linearly in the $\hat{x}$ or $\hat{y}$ direction. If $E_1 = E_1 \neq 0$, the resulting wave is polarized linearly with a polarization angle $\phi$, which can be determined as

$$\phi = \tan^{-1} \frac{E_2}{E_1} \tag{18}$$

Any other combinations lead general to the elliptical polarization, which can be a circular polarization as a specific case, when both orthogonal components have the same amplitude $E_1 = E_2 = E_0$ and the phase shift between both components is $\frac{\pi}{2}$. The form of this field is then

$$\vec{E} = E_0(\hat{x} + \mathrm{j}\hat{y})e^{-jk_0 z} \tag{19}$$

Hence there are two possibilities of the phase shift $\frac{\pi}{2}$ in both directions right and left, we can distinguish two circular wave arrangement. The right-hand circularly polarized wave (RHCP) can be determined by the right hand, when the finger points in the direction of propagation and the fingers point in the direction of rotation of the electric field vector. By other words, a wave is RHCP polarized, if it travels from the observer and its rotation is clockwise.

When the vector rotates in the opposite manner, the wave is left-hand circularly polarized wave (LHCP), rotation from the observer is counter-clockwise and the field can be described as

$$\vec{E} = E_0(\hat{x} - \mathrm{j}\hat{y})e^{-jk_0 z} \tag{20}$$

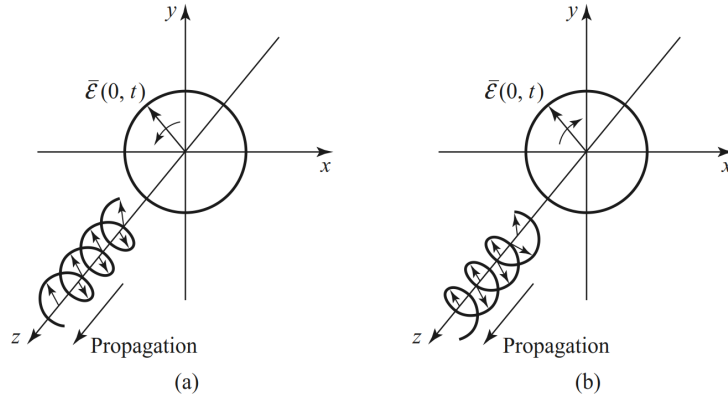The illustration of both RHCP and LHCP is shown in the Fig. 4



Figure 4: RHCP (a) and LHCP (b) polarized electromagnetic waves, taken from [7].

### 3.2.1 Characteristics of the circular polarization

There are a few significant advantages of the circular polarization compared to the linear polarization. When travelling through the atmosphere, change in the polarization of the wave occurs. This effect, which is called Faraday rotation, is stronger when the travelling path is long and it would be significant for the long distance communication, like satellite connection or navigation services.

When a electromagnetic wave travels through the atmosphere, particular the ionosphere, the Faraday rotation causes a rotation of the plane of the polarization, which is linearly

8

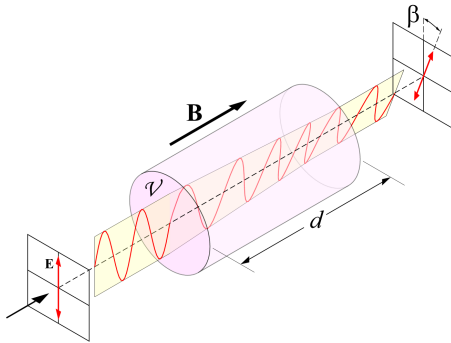proportional to the magnetic field in the direction of propagation. This situation shows Fig. 5.



Figure 5: Illustration of the Faraday effect, taken from [6].

The angle change $\beta$ can be described

$$\beta = VBd \tag{21}$$

where $V$ is a Verdet constant, $B$ is a magnetic field and $d$ is a length path.

If the electric field is polarized differently than the receiving antenna, the available power will be less than in case of alignment of the wave and the antenna. This angle misalignment causes, in the case of ideal linearly polarized system, a polarization loss, which can be described for with a polarization loss factor (PLF) as

$$\text{PFL} = \cos^2 \phi \tag{22}$$

where $\phi$ is a angle difference between the wave and the receiving antenna. If the wave and the antenna are polarization matched, PLF=1, and there is no polarization power loss, on the other side, if PLF=0, no power is transmitted due to this polarization mismatch. If we consider a situation with linearly polarized wave and circularly polarized receiving antenna, the loss mismatch loss will be PLF=0.5=-3 dB, because of receiving only one component of the two orthogonal components, no matter what angle they are rotated to each other.

Another reason for using the circular polarization is that it suppresses very effectively multi-path interferences caused by reflections from the objects, particular the Earth, since the right-hand polarization change in the left-hand polarization (and vice versa) when the wave reflects.

Because of the nature of the circular polarization, the both antennas need not be perfectly orientated in the appropriate angle to each other when compared to the linear polarization, where significant mismatch losses would occur.

For the above advantages the circular polarization is favourably used by the global navigation satellite system (GNSS), which use right-hand circular polarization, or another satellite communication, like TV broadcasting or space telemetry and could be attractive for many other wireless systems. Because of the good resistance to the position misalignment, circular polarization can be favourably used for radio frequency identification (RFID), where the position of the RFID chip antenna is not constant.

9

### 3.2.2 Axial ratio

One of the parameters describing the polarization state of the wave is an axial ratio. It can be determined from the polarization ellipse, which is described by the rotating electric field vector. An example of such ellipse is shown in the Fig. 6.
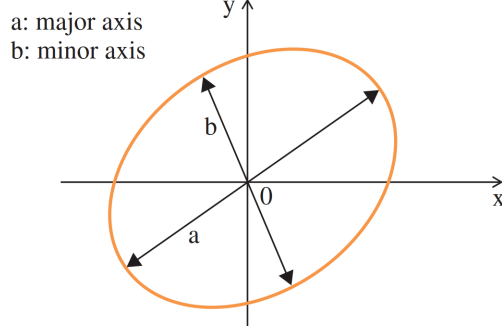


Figure 6: The electric intensity vector describing polarization ellipse, taken from [5].

Using the arrangement in the Fig. 6 the axial ratio $R$ can be defined

$$|R| = \frac{a}{b} = \frac{\text{major axis length}}{\text{minor axis length}} = \frac{E_{\max}}{E_{\min}} \tag{23}$$

And with the value in the decibels

$$|R_{\mathrm{dB}}| = 20 \log |R| \tag{24}$$

Axial ratio is an important parameter for measuring of the circular polarization. For circular polarization, when the polarization ellipse become circle, the value of axial ratio is $R$=1, while for linear polarization, the ratio is $R=\infty$. Usually $R$ is required to be below 3 dB for circular polarized antenna [5].

### 3.2.3 Missmatch loss

The mismatch loss for any angular position between major axes of the electromagnetic wave and the receiving antenna both with the general elliptical polarizations can be calculated [12] as

$$\mathrm{PFL(dB)} = 10\log\left[\frac{1 + \rho_w{}^2\rho_A{}^2 + 2\rho_w\rho_A\cos 2\phi}{(1 + \rho_w{}^2)(1 + \rho_A{}^2)}\right] \tag{25}$$

where $\rho_w = (R_w + 1)(R_w - 1)$ is the circular polarization ratio of the wave and $\rho_A = (R_A + 1)(R_A - 1)$ is the circular polarization ratio of the receiving antenna.

## 3.3  Circularly polarized antennas

Only a few types of antenna have inherent circular polarization, for example helix antenna, spiral antenna or modified patch antennas. Other antennas are usually distinguish by the linear polarization and for creating of the circular polarization an arrangement of two linearly polarized antennas with phase shifting is used.

### 3.3.1  Helix antenna

Helix antenna consist of wire wounded in the form of screw. The parameters of the helix antenna determines its characteristics and they include the diameter $D$ of one turn, the vertical interval $S$ between turns, the pitch angle $\alpha$ or the number $N$ of turns. Depending on these attributes the helix antenna can operate in three different modes, which are shown in Fig. 7:

- **Normal mode**: occurs when the diameter of the spiral is relatively small compared to the wavelength ($D < 0.1\lambda$). The radiation of this helix is omni-directional, similar to the one of the dipole.

- **Axial mode**: appears when the cirfumference of the spiral is comparable to one wavelength. The radiation pattern has its maximus in the axis of the helix.

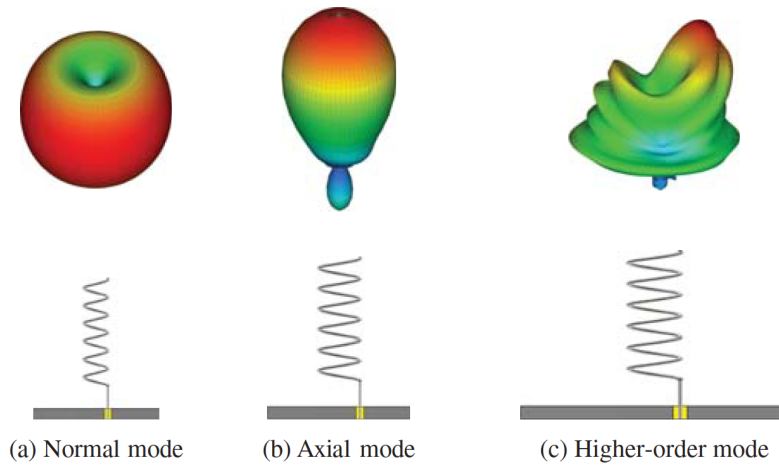- **Higher-order mode**: occurs when circumference exceed one wavelength $\lambda$



(a) Normal mode      (b) Axial mode      (c) Higher-order mode

Figure 7: Radiating modes of the helix antenna, taken from [5].

### 3.3.2  Self-complementary antenna

The spiral self-complementary antennas are frequency independent antennas, which can create a circular polarization in a wide frequency range. The impedance matching is frequency independant since the structure consists of two complementary (slot and metal) surfaces of the same area, as can be seen in Fig. 8. The relation between the impedances of these both shapes describes the Babinet's principle [8]

$$Z_{\mathrm{metal}}Z_{\mathrm{slot}} = \frac{Z_0{}^2}{4} \tag{26}$$

From this equation the impedances are $Z_\text{metal} = Z_\text{slot} \doteq 188.5\Omega$.

The operating frequency range is limited by the geometrical arrangements. The lowest operating frequency is limited with the input terminal distance $d$ and the lowest operating frequency is bounded with the antenna diameter $2D$.
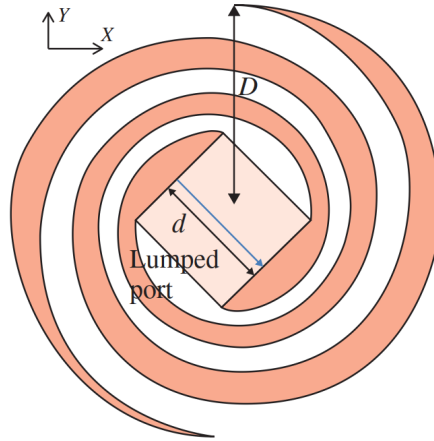


Figure 8: Log-spiral wideband RHCP antenna, taken from [5].

### 3.3.3 Patch antenna

Another arrangement can be patch antennas with a single feed, which use perturbations of the shape for exciting the orthogonal modes in the right proportion, using truncated corners, slits or another shapes. Fig. 9 shows two examples of the circularly polarized patch antennas with a slot.
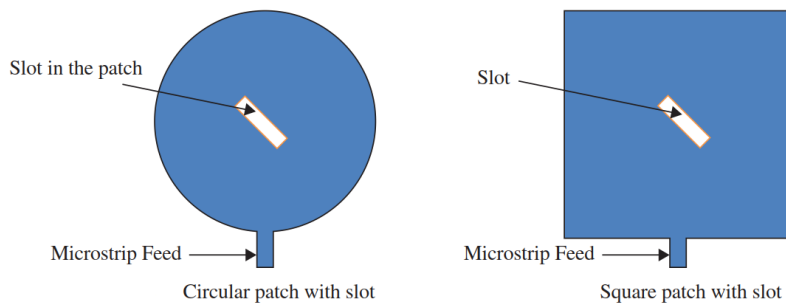


Figure 9: Examples of patch antennas with a circular polarization, taken from [5].

Another structure for exciting of a circular polarization can be also used, but the antennas need to have an feeding structure, like in Fig. 10, which divides the power into two orthogonal modes and provides a phase shift of 90°. This can complicate the design and the accuracy of the assembly and in addition the power dividers and the phase shifters are usually narrow-band.
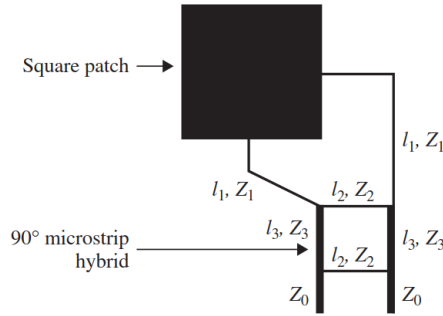
Figure 10: CP patch antenna with a 90° phase shifter, taken from [5].

# 4 Antenna measurements

Because of the complex structure a lot of antennas can not be investigated analytically and the measurement is needed for approving of the developed antenna, where the theoretical assumptions should be validated. The convenient method for performing antenna measurement is with the test antenna as a receiving antenna, but also the inverse arrangement is possible due to the reciprocity of the antennas. Hence the right measurement should occur in the free space with no reflection and other disadvantage influences and interferences and the outdoor is not very convenient for measurement for its weather impact, the measurements are often done in an anechoic chamber. The anechoic chamber provide an environment, where the electromagnetic interferences are minimized, the reflections from the walls are suppressed with a special absorption material with suitable shaping based on the pyramidal structures, where the waves multiply reflects and their energy is successively absorbed.

For the correct results, the measurement needs to be done in the far field region, thus the mutual distance needs to ensure the far field region for both antennas.

The usually measured antenna parameters are gain, radiation patterns in more planes, reflection coefficient and polarization.

## 4.1 Gain measurement

Most of the gain measurement are based on the Friis transmission formula, which can be expressed in logarithmic units as

$$P_r = P_t - L_0 + G_t + G_r \tag{27}$$

where $P_r$ is an received power [dBm], $P_t$ transmitted power [dBm], $G_r$ gain of the receiving antenna [dB], $G_t$ gain of the transmitting antenna [dB] and $L_0$ is free space loss (FSL) at given distance $R$ and for given wavelength $\lambda$, which is given by

$$L_0 = 20 \log \frac{4\pi R}{\lambda} \tag{28}$$

All the antenna measurements are subject to errors, for the valid results it is need to give an exceptional attention to the frequency stability of the measured system, the antennas'

placing in the far field region, antennas' alignment in the boresights, impedance matching and polarization matching and to the minimization of the multipath propagation.

There are three basic methods for gain measurements [28]:

- **Two identical antenna method** uses two identical antennas as receiving and transmitting antenna $(G_t = G_r)$. Their gain reduces from Equation 27 to

$$G_r = G_t = \frac{1}{2}P_r - P_t + L_0 \tag{29}$$

- **Three different antenna method** uses a three different antenna, which all their combination are used to determine the gain of each of the three. We get then 3 equations with 3 unknown gains, from which the each gain $G_1$, $G_2$ and $G_3$, can be easily derived.

$$G_1 + G_2 = P_{r1} - P_{t2} + L_0$$

$$G_2 + G_3 = P_{r2} - P_{t3} + L_0 \tag{30}$$

$$G_1 + G_3 = P_{r1} - P_{t3} + L_0$$

  This method is the most accurate of all described methods. It is also the most universal method for antenna measurements since there is no need to know gains of the individual antenna.

- **Reference antenna method** is the easiest method for antenna measurement, which requires to have a reference antenna with the known gain $G_r$. The received power by the reference antenna is then compared with the power received with the measured antenna, while the transmitting antenna is the same for both measurements. The received powers with the reference antenna $P_{r1}$ and with the measured antenna $P_{r2}$ are given by

$$\begin{aligned} P_{r1} &= P_t - L_0 + G_t + G_r \\ P_{r2} &= P_t - L_0 + G_t + G_x \end{aligned} \tag{31}$$

Combining these both equations the gain of the measured antenna $G_x$ is given by

$$G_x = P_{r2} - P_{r1} + G_r \tag{32}$$

For measuring of the designed antennas this method will be used for its simplicity.

## 4.2   Reflection coefficient measurement

The reflection coefficient describes a impedance matching of the antenna. For the maximal power transfer between a generator and an antenna a conjugate match is usually desired as described in Section 2.1. From the measured reflection coefficient by a spectral analyser, the input impedance can be expressed as

$$Z_{in} = Z_0 \left[ \frac{1+\Gamma}{1-\Gamma} \right] \qquad (33)$$

For a good antennas a reflection coefficient -10 dB and lower is required.

## 4.3 Polarization measurement

For the description of the antenna's polarization, the polarization ellipse and the sense of the rotation are used. The tested antenna is usually used as a transmitting antenna and the method requires a testing linearly polarized antenna, usually a dipole or horn antenna. The arrangement of both antennas and the rotation sense can be seen in Fig. 11.



Antenna under test

Rotate test probe
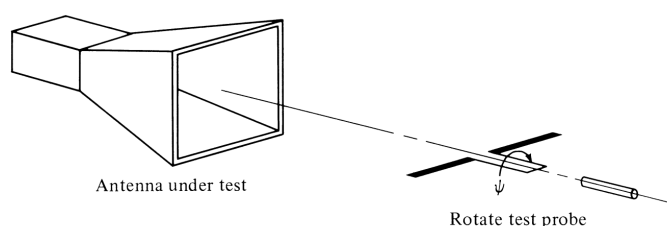
Figure 11: Measurement of the polarization, taken from [8].

If the test antenna is linearly polarized, the voltage response is determined by $\sin \psi$, where $\psi$ is the rotation angle of the probe to a reference direction, and the pattern has an eight-shape as can be seen in Fig. 12, whereas the minimum of the pattern corresponds to the orthogonal arrangement of the both antennas.



Linear        Elliptical        Circular
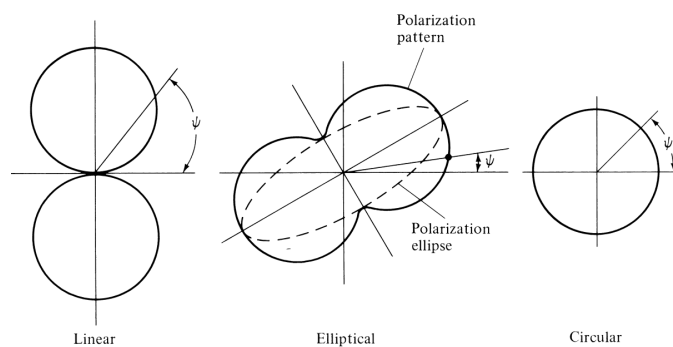
Figure 12: Typical polarization patterns for different polarizations of the tested antenna, taken from [8].

# 5 Circular waveguide

The circular waveguide can be an alternative to the rectangular waveguides. It consist of a hollow, round metal pipe with an inner radius $a$. Because of the cylindrical geometry, cylindrical coordinates should be applied, which can be described using radial ($\rho$), azimuthal ($\phi$) and vertical ($z$) coordinates. The geometry of such is shown in the fig. 13
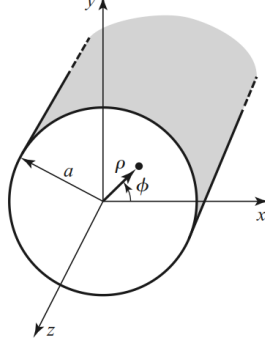


Figure 13: Geometry of the circular waveguide, taken from [7].

Due to the cylindrical geometry, the manufacturing process can be done easier and with more accuracy than of the the rectangular waveguides, which have sharp edges.

As all waveguide the circular waveguide also makes low-loss transmission, better than of coaxial cable. To enable waves to travel through the waveguide, the diameter must be large enough for the lowest possible (dominant) mode. In the circular waveguide two transverse mode types can propagate:

1. **Transverse electric (TE) modes**, which has no electric field in the direction of propagation.

2. **Transverse magnetic (TM) modes**, which has no magnetic field in the direction of propagation.

We can distinguish these mode to according to the space arrangement of the electromagnetic field, describing the modes $TE_{nm}$ and $TM_{nm}$, where $n$ refers to the number of circumferential ($\phi$) variations and $m$ refers to the number of radial ($\rho$) variations.

The transverse electromagnetic (TEM) modes can not propagate in the waveguides, since TEM modes require two or more conductors to be excited.

Each mode has its own cutoff wavelength $\lambda_c$, below which the electromagnetic wave can not propagate and which corresponds to the dimensions of the waveguide.

The first mode (dominant mode) for a circular waveguide is the $TE_{11}$.

## 5.1 TE modes in circular waveguide

Transverse electric modes has only magnetic field along the direction of propagation and no electric field in the direction od propagation. The basic geometry with corresponding vectors is depicted in Fig. 14.
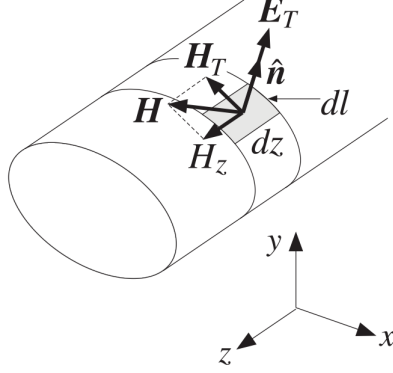


Figure 14: Geometry of the circular waveguide [10].

Hence, the conditions $E_z = 0$ and $H_z \neq 0$ and the transverse electric field is then determined by the transverse magnetic field $H_T$ we obtain field components as [10]

$$\nabla_{\mathrm{T}}^2 H_z + k_{\mathrm{c}}{}^2 H_z = 0$$

$$H_{\mathrm{T}} = -\frac{j\beta}{k_{\mathrm{c}}{}^2}\nabla_T H_z \tag{34}$$

$$E_{\mathrm{T}} = \eta_{\mathrm{TE}} H_{\mathrm{T}} \times \hat{z}$$

Where $\beta$ is the propagation constant defined as $\beta = \frac{2\pi}{\lambda_g}$, $\eta_{\mathrm{TE}}$ the wave impedance and $k_c$ is a cutoff wave number given by

$$k_{\mathrm{c}}{}^2 = \omega^2 \epsilon \mu - \beta^2 \tag{35}$$

Since the cylindrical coordinates are used, solution of the wave equation can be found with the Bessel's functions (derivation can be found e.g. in [7], p. 122-124) in the form

$$\rho^2 \frac{\mathrm{d}^2 R}{\mathrm{d}\rho^2} + \rho \frac{\mathrm{d}R}{\mathrm{d}\rho} + (\rho^2 k_{\mathrm{c}}{}^2 - n^2)R = 0 \tag{36}$$

The solution is

$$R(\rho) = CJ_n(k_{\mathrm{c}}\rho) + DY_n(k_{\mathrm{c}}\rho) \tag{37}$$

where $J_n(x)$ is the Bessel function of first kind and $Y_n(x)$ is the Bessel function of second kind.

The graph of the Bessel's functions of the first kind are shown in Fig. 15.
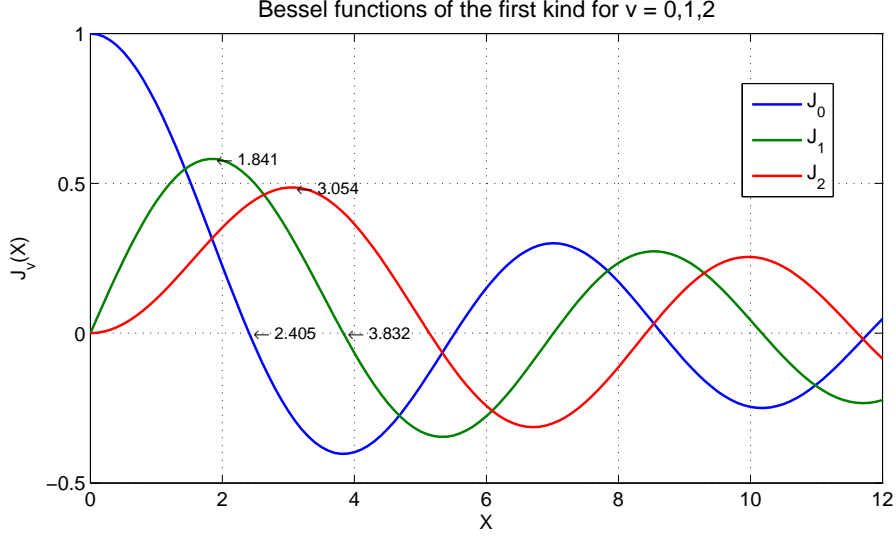


Figure 15: Bessel's functions of the first kind with first extreme values marked.

The propagation constant of the $\text{TE}_{nm}$ mode is given by

$$\beta_{nm} = \sqrt{k^2 - k_c{}^2} = \sqrt{k^2 - (\frac{p'_{nm}}{a})^2} \tag{38}$$

where $p'_{nm}$ are the roots of the derivative of the Bessel's function $J_n$, so that $J'_n(p'_{nm}) = 0$. The cutoff frequency $f_{\mathrm{c}nm}$ is then

$$f_{cnm} = \frac{k_c}{2\pi\sqrt{\mu\epsilon}} = \frac{p'_{nm}}{2\pi a\sqrt{\mu\epsilon}} \tag{39}$$

where $\mu$ is permeability and $\epsilon$ permittivity of the medium.

The values of $p'_{nm}$ [7] for $n$=0, 1 and 2 are in Table 1.

| n [–] | $p'_{n1}$ | $p'_{n2}$ | $p'_{n3}$ |
|---|---|---|---|
| 0 | 3.832 | 7.016 | 10.174 |
| 1 | 1.841 | 5.331 | 8.536 |
| 2 | 3.054 | 6.706 | 9.970 |

Table 1: Values of $p'_{nm}$ of the Bessel's function derivative for TE modes, taken from [7].

The first mode (dominant mode) is that mode with the lowest $p'_{nm}$, which is in the circular waveguide the $\text{TE}_{11}$ mode with $p'_{n1} = 1.841$, so the cutoff frequency will be

$$f_{cnm} = \frac{1.841}{2\pi a\sqrt{\mu\epsilon}} \tag{40}$$

The next TE modes supported in the circular waveguide are $\text{TE}_{21}$, $\text{TE}_{01}$, etc.

18

The field distribution of the TE modes illustrates fig. 16
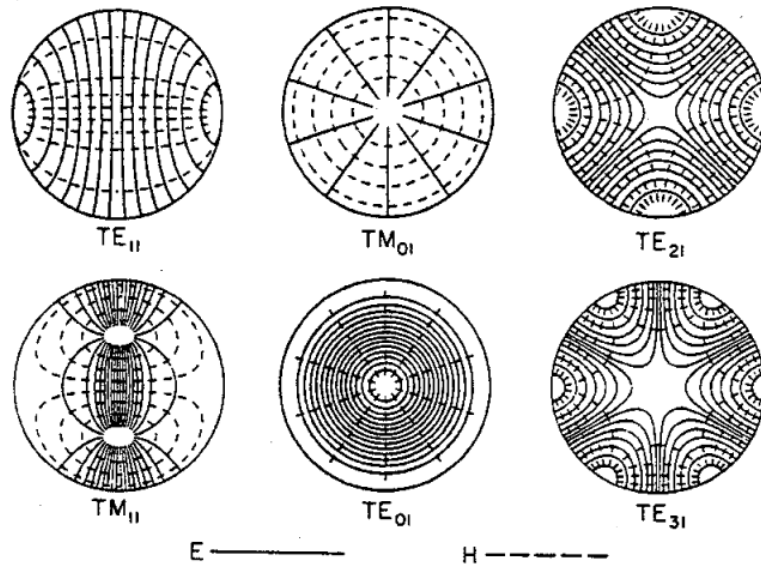


Figure 16: First six transverse modes of a circular waveguide, taken from [13].

## 5.2 TM modes in circular waveguide

The second mode type propagating in the circular waveguide can be transverse magnetic modes. Their magnetic field fulfils the condition $H_z = 0$ and from the boundary condition at the walls of the waveguide we get $E_z(\rho = a, \phi) = 0$.

Similar as Equations 34 we get [10]

$$\nabla_T{}^2 E_z + k_c{}^2 E_z = 0$$

$$E_T = -\frac{j\beta}{k_c{}^2}\nabla_T E_z \tag{41}$$

$$H_T = \frac{1}{\eta_{TM}}\hat{z} \times E_T$$

For the cutoff wave number we get

$$k_c = \frac{p_{nm}}{a} \tag{42}$$

where $p_{nm}$ is the root of the Bessel's function $J_n(x)$, therefore $J_n(p_n m) = 0$.

The cutoff frequency $f_{cnm}$ is

$$f_{cnm} = \frac{k_c}{2\pi\sqrt{\mu\epsilon}} = \frac{p_{nm}}{2\pi a\sqrt{\mu\epsilon}} \tag{43}$$

First three values of Bessel's function $p_{nm}$ [7] shows table 2.

| n [−] | $p_{n1}$ | $p_{n2}$ | $p_{n3}$ |
|-------|----------|----------|----------|
| 0 | 2.405 | 5.520 | 8.654 |
| 1 | 3.832 | 7.016 | 10.174 |
| 2 | 5.135 | 8.417 | 11.620 |

Table 2: Values of roots $p_{nm}$ of the Bessel's function, taken from [7]

From the table the first TM mode can be derived as $TM_{01}$ and the following modes $TM_{11}$, $TM_{21}$, etc.

The summary of the individual TE and TM modes in the circular waveguide with their cutoff frequencies normalized to the dominant $TE_{11}$ mode is shown in Fig. 17.
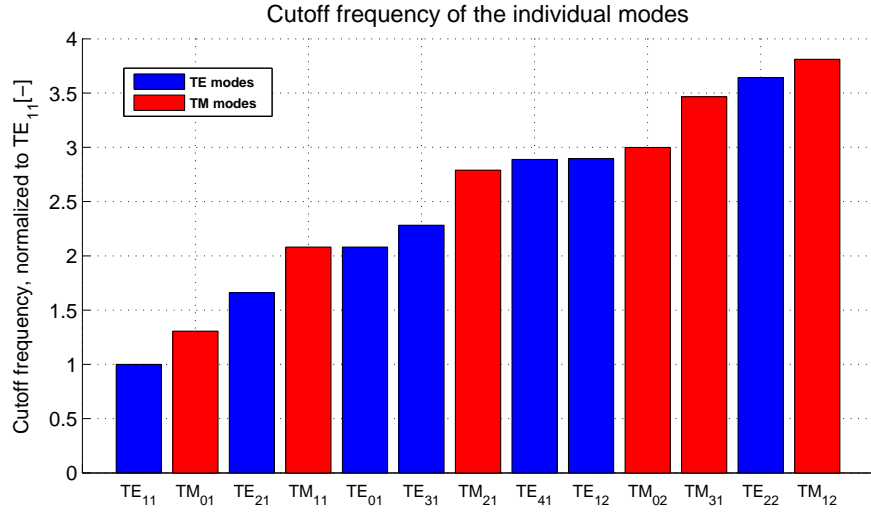
Figure 17: Normalized cutoff frequencies of the TE and TM modes in the circular waveguide

## 5.3 Wavelength in the waveguide

The wavelength in the waveguide is defined as the distance between two planes with the same phase along the waveguide. The guide wavelength $\lambda_g$ is always longer than the wavelength in the freespace and it is given by [7]

$$\lambda_g = \frac{2\pi}{\beta} = \frac{2\pi}{\sqrt{k^2 - (\frac{p_{nm}}{a})^2}} \tag{44}$$

# 6 Polarizers

Polarizers are devices used not only in the radio frequency engineering, but also in the optical fields. The main goal of polarizer is to convert one type of polarization to another one, typically it is from linear to circular polarization or vice versa, being reciprocal in its function. The circular polarization can be created by two orthogonal waves, which are shifted by 90°. Hence, there are two conditions that needs to be fulfilled for the right function of the polarizer. First, the linearly polarized signal must be divided into orthogonal components with an identical amplitude. The second condition is to make these orthogonal components shifted in phase at 90° between them. In the state of art more types of waveguide polarizers are used, whereas the most common polarizers are polarizers with irisses [1], [2], with a metal [14] or with a dielectric [15] septum or with other perturbation elements.

## 6.1 Iris polarizer

Iris polarizers are one of the classical arrangements of the polarizer in the waveguides. Polarizers with irises can be found in [1], the matematical description using transmission line theory and describing the irises by capacitance and inductance is to be found in [2]. The very thin irises, which are usually designed in the circular or rectangular waveguides, can be circle segments or of elliptical shape. The irises may have different dimensions and separation between themselves, but they are generally arranged at regular intervals. The principle of these irises is to vary transverse dimensions in the sections of the waveguide due to the the discontinuities of capacitive type for one polarization (e.g. $TE_{01}$ in the rectangular waveguide) and inductive type for the other mode (e.g. $TE_{10}$ in the rectangular waveguide), and so produce a phase difference between two orthogonal components of the field. With corresponding propagation constants $\beta$ and $\beta'$ the phase shift $\Delta\phi$ at each iris with a distance $l$ between two irises (as can be seen in Fig. 18) is given by

$$\Delta\phi = (\beta' - \beta)l \tag{45}$$

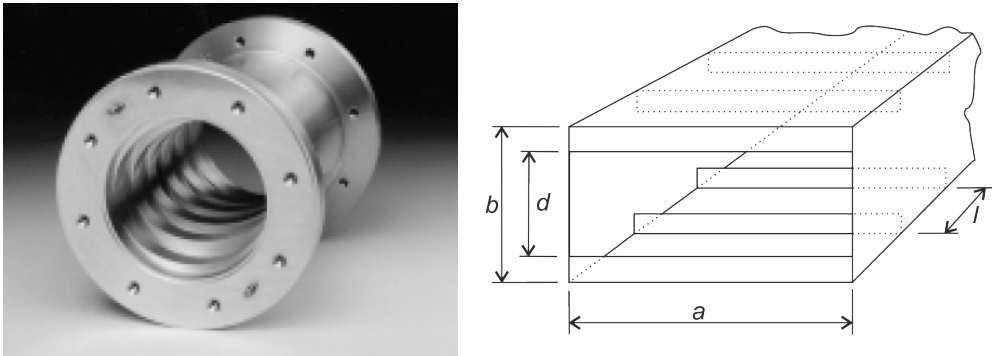The total shift at the end of the polarizer is a sum of the partial shifts generated by each iris.



Figure 18: Polarizer a) in the circular waveguide with elliptical irises, taken from [1] and b) in the rectangular waveguide with rectangular irises.

Because of the complicated arrangement, the manufacturing process can not be realised undivided and is very technically demanding. Iris polarizers are usually made of separate longitudinal segments or of two longitudinal halves, equipped with suitable flanges for screwing them together. The assembly needs to be carried out carefully to avoid undesired deformation and the manufacturing inaccuracies can result.

If there is a cutting in the longitudinal plane for better manufacturing, different insertion losses of the two modes can occur, since for one modes the currents flow in the direction of the cutting and for the the another mode they flow perpendicular to the cutting [1].

## 6.2  Septum polarizer

The septum polarizer consists of a stepped conductive septum in the middle of the waveguide, dividing it into two half-circular parts. Detail of the septum polarizer is depicted in Fig. 20
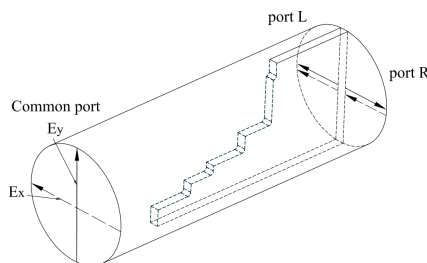


Figure 19: Schematics of the septum polarizer, taken from [14].

The parallel section is divided equally by the septum into the two half-circular waveguides, which have another cutoff frequency. The wavelength for the perpendicular component is shorter. When the difference in length is 90°, the both components arrive in phase at the input and according to the sense of circular polarization (RHCP or LHCP), they add together or cancel each other.

Another arrangement uses a dielectric septum, which is placed at the centre of the waveguide, usually at 45° to the incident electric field vector $E_0$. This septum, shown in Fig. 20, can introduce circular polarization, since the dielectric constants $\epsilon_x$ and $\epsilon_y$ for two orthogonal polarizations $E_x$ and $E_y$ in $x$ and $y$ directions are different and so the propagation constants $\beta_x$ and $\beta_y$. Choosing a suitable polarizer length a desired 90° phase shift can be realized at the output. This polarizer is characterized by lower reflections than the polarizer with a metal septum and the phase difference can be easily improved by adjusting the length of the dielectric septum [15].
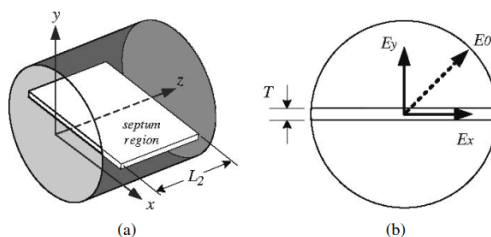


Figure 20: Dielectric septum in a) general view and b) front view, taken from [15].

## 6.3 Grid polarizer

Another arrangement for creating circular polarization proposed by Lee [3] uses a grid as a polarizing element. It uses a wire grid slanted at 45° to the vertical electric field vector generated by the probe. At the grid, the vertically polarized wave is divided into two polarizations, one parallel and one perpendicular to the wire, while the perpendicular component gets through the grid, it will be reflected with 180° delay from the back-short, which is $\frac{\lambda_g}{4}$ from the grid and therefore is in phase with the incident wave. The parallel component is reflected from the wire with a 180° phase shift and due to opposite direction of the vector, a orthogonal polarization is generated. Phase delay section of length $\frac{\lambda_g}{8}$ then provides a 90° phase delay of both polarizations and thus a circular polarization occurs. This arrangement of the polarizer with reflection principle is characterized with a compact size about 0.8 $\lambda_g$ and the sense of polarization can be easily changed with a grid rotation at 90°, so as it reflects the other electrical component. For making radiating characteristics more symmetrical and side lobes being suppressed better, which are for needed for certain applications, a structure at the output can be designed, as described in Section 7.
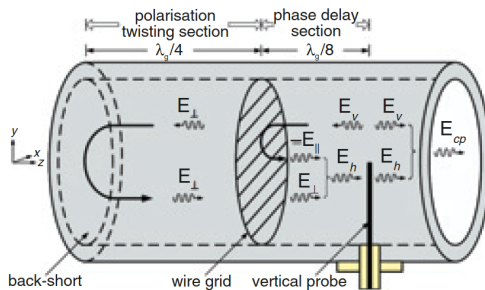


Figure 21: Schematics of the grid polarizer, taken from [3].

## 6.4 Polarizers with loading plates

Other technique for producing circular polarization is a arrangement with dimensional perturbation distributed along a waveguide section. Such embodiment publishes e.g. patent US 4,523,160 [16], which contains proposal of an arrangement in square, circular or crossed waveguides. Polarizers designed there comprise beside a conductive plates, which are positioned in opposite sides of the waveguide, so the internal shape (when circular waveguide is considered) is changed from circular to somewhat elliptical shape, which has horizontal dimension smaller than the vertical dimension as shown in Fig. 22. The loading on opposite sides of the waveguide are identical to avoid excitation of the non-symmetrical modes. The patent proposes using another layer of the dielectric material above the conductive plates to improve performance of such polarizer with achieving wider bandwidth and shortening the length of the overall polarizer.

Because of the compact shape and possibility to make this type of polarizer without demanding milling technique, which can be easily printed using a 3D printer, polarizers of this art will be designed and created.
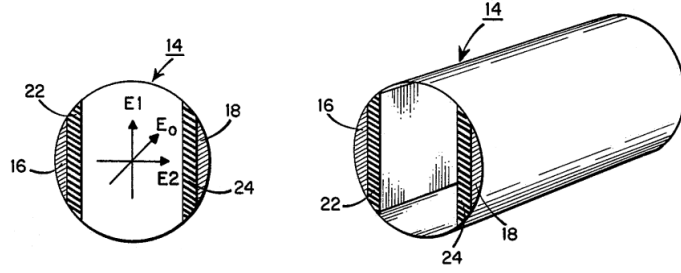
Figure 22: Schematics of a polarizer with plates, taken from [16].

## 6.5 Elliptical polarizer

Similar arrangement like the polarizer in the circular waveguide can be developed in the elliptical waveguide. This type of polarizer is described in [?] The principle is also very similar to the circular polarizer, but there are no flats at opposite sides of the waveguide and the pertrubation is done with the elliptical cross-section, at which two orthogonal modes are being excited by a appropriate feeding, which is turned an angle 45° to the longitudinal axis of the waveguide as in Fig. 23.

When a dominant $TE_{11}$ mode is being propagated in a elliptical waveguide, the original $TE_{11}$ mode will split into two even and odd components $_eTE_{11}$ and $_oTE_{11}$, which have different characteristics, propagation constants or cutoff frequencies. With a suitable length of the polarizing section, a phase shift 90° can be achieved and created the circular polarization.
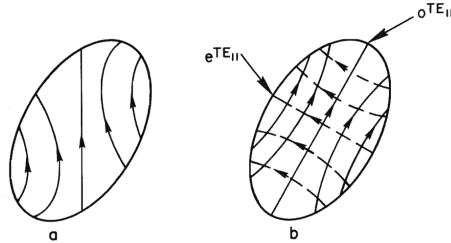


Figure 23: Generating of orthogonal modes in the elliptical waveguide, taken from [11].

Because of the complex shape and demanding forming, this arrangement is very suitable for 3D printing and the second polarizer design will used the elliptical shape, which elliptical cross-section causes an phase shift of the orthogonal modes similar to the above mentioned design of the polarizer with the conductive plates.

# 7 Dual-mode section

When leaving the output aperture to be opened waveguide, only dominant $TE_{11}$ mode will be excited at the circular horn aperture. Because of the inconvenient properties of the electric field vector of the dominant $TE_{11}$ mode, which is not symmetric in both $E$ and $H$ planes, the radiating patterns are not equal in the $E$ and $H$ planes, the electric field components can be written as [7]

$$E\rho = \frac{-j\omega\mu}{k_c^2\rho}A\cos\phi J_1(k_c\rho)e^{-j\beta z} \tag{46}$$

$$E\phi = \frac{j\omega\mu}{k_c}A\sin\phi J_1'(k_c\rho)e^{-j\beta z} \tag{47}$$

For creating a radiation pattern with a good axial symmetry, providing beam width equalization in both $E$ and $H$ planes, lower side lobe level at about -40 dB and low level of cross-polarization of the opened waveguide a structure realizing excitation of the higher modes can be employed at the waveguide opening. Such a structure changes the field distribution at the aperture to be more homogeneous and closer to the Huygen's source, which electric field lines are parallel in the $E$ plane and no cross-polarization components exist in the $H$ plane. Such electric field distribution is advantageously used for feeding of the reflector antennas and the horn used for this improvement are called dual mode horns.

The basic principle of such horns is to excite higher mode $TM_{11}$ besides the dominant mode $TE_{11}$ in the transition section and with appropriate horn length making $TE_{11}$ and $TM_{11}$ reach the projecting aperture in phase, so the side lobe radiating is suppressed. The horn antenna using this method of balancing of the modes, is known as dual-mode horn. The easiest method, which may be employed for generating the higher mode is a change in the dimensions of the waveguide. When a symmetrically stepped widening of the waveguide occurs in the path of the electromagnetic wave, the right designed larger waveguide section supports a higher mode propagation, while the section with smaller radius due to its radius smaller for propagation of the higher $TM_{11}$ mode, can not, the dominant mode will be decomposed in the wider section into the $TE_{11}$ and $TM_{11}$ at the discontinuity. When properly phased at the aperture, what is given by the the appropriate choice of the input waveguide diameter, the step widened section area diameter and the output horn length, the $TM_{11}$ mode cancels the $\phi$ component of the magnetic field due to the $TE_{11}$ mode at the aperture, which causes both $H_\phi$ and $E\phi$ to vanish [9]. Hence the circular waveguide has an axial symmetry, $TE_{mn}$ or $TM_{mn}$ modes with $m>1$ will not be excited.

Fig. 24 shows the distribution of electric field vector at the aperture and the resulting pattern after combining both $TE_{11}$ and $TM_{11}$ at the aperture, wherein the two field near the boundary oppose one another.

There are more types used for the dual-mode excitation, one of the first who studied the improvments of the antenna characteristics, in particular side lobe level, using higher mode excitation for symetrizating of the electromagnetic field was Phillip D. Potter, who patented a Dual mode horn antenna in 1963 [18].
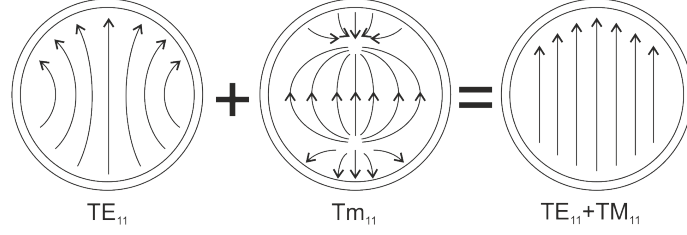
Figure 24: Combination of electric and magnetic mode types to creating a Huygen's source.

## 7.1 Potter horn

The design of conical antenna horn, called after his inventor Potter horn, is illustrated in Fig. 25. Potter horn has a step transition from the feeding waveguide diameter to the such diameter, that is enough large to can excite the higher mode and make possible to support both waveguide modes. When correctly phased, these both modes has their phase centers coincident at the aperture. This phase centering is done with a phasing section in the horn. As a result side lobe level lower than -30 dB can be achieved in the electric field plane ($E$ plane), while leaving the magnetic field plane ($H$ plane) unaffected.
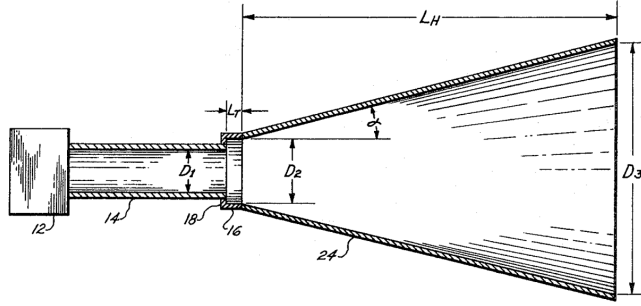


Figure 25: Potter horn for dual mode excitation at the aperture, taken from [18].

The electric fields of the $TE_{11}$ mode are given [19] as follows

$$E_{\theta H} = -\frac{\omega\mu}{2R}\left(1 + \frac{\beta_{11H}\cos\theta}{k}\right)J_1(K_{11H}a)\left[\frac{J_1(ka\sin\theta)}{\sin\theta}\right]\sin\phi e^{-jkR}$$

$$E_{\phi H} = -\frac{ka\omega\mu}{2R}\left(\frac{\beta_{11H}}{k} + \cos\theta\right)J_1(K_{11Ha})\left[\frac{J_1'(ka\sin\theta)}{1 - \left(\frac{k\sin\theta}{K_{11H}}\right)^2}\right]\cos\phi e^{-jkR} \quad (48)$$

where $a$ is aperture radius, $J_1$ first order Bessel function of the first kind, $J_1'$ first derivative of $J_1$, $K_{11H}a$=1.841 first root of $J_1'$, $R$ distance from the aperture center $\theta$ elevation angle, $\phi$ azimuth angle, $\beta_{11H} = \sqrt{k^2 - K_{11H}^2}$ phase constant of the $TE_11$ mode and $k = j\omega\sqrt{\mu_0\epsilon}$) free-space propagation constant.

27

The electric fields of the $TM_{11}$ mode are given [19] as

$$E_{\theta E} = -\left(\frac{kaK_{11E}}{2R}\right)\left(\frac{\beta_{11E}}{k} + \cos\theta\right)\left[\frac{J_1'(K_{11E}a)}{1 - \left(\frac{K_{11E}}{k\sin\theta}\right)^2}\right]\left[\frac{J_1(ka\sin\theta)}{\sin\theta}\right]\sin\phi\, e^{-jkR} \tag{49}$$

$$E_{\phi E} = 0$$

where $K_{11E}a{=}3.832$ is the first root of $J_1$ and $\beta_{11E} = \sqrt{k^2 - K_{11E}^2}$.

Equations 48 and 49 can be combined and simplified as:

$$E_{\theta T} = \left[\left(1 + \frac{\beta_{11H}}{k}\cos\theta\right) - \alpha\frac{\left(\frac{\beta_{11E}}{k}\right) + \cos\theta}{1 - \left(\frac{K_{11E}}{k\sin\theta}\right)^2}\right]\left[\frac{J_1(ka\sin\theta)}{\sin\theta}\right] \tag{50}$$

where $0 \le \alpha \le 1$ is a constant defining the relative power being carried in the $TE_{11}$ and $TM_{11}$ modes. As in [19], there is a specific case for value of $\alpha$, that is $\alpha = 0.653$, when the half-power beam widths (HPBW) in the $E$ plane and $H$ plane are equalized, that results in the minimal side lobes (up to -40 dB).

## 7.2    Pickett-Potter horn

Another variant of the Potter horn was presented by H.M. Pickett [20] in 1984. Pickett proposed a simplified version of the conventional Potter horn, whereas he removed the phasing section as shown in Fig. 26. The excitation of the $TM_{11}$ mode and his matching with the dominant $TE_{11}$ mode is thus done by the step discontinuity from the waveguide section to the widening. This discontinuity generates a small fraction of the $TM_{11}$ mode, while the $TE_{11}$ mode can further propagate. The radiation characteristics are similar to the of the Potter horn, but there is a disadvantage of the lower bandwidth when compared to the Potter horn, because the mode matching is done without the phasing section. This disadvantage of the Pickett-Potter horn, which is a result of the inherent frequency dispersion at the step transition, can be suppressed with insertion of a dielectric ring at the discontinuity, as in [23]. Despite this disadvantages, the Pickett-Potter horn can be manufactured easily, while the desirable properties of low side lobe level are sufficient for most of the applications. Another analysis of the Pickett-Potter horn can be found in [21], [22] or [24].
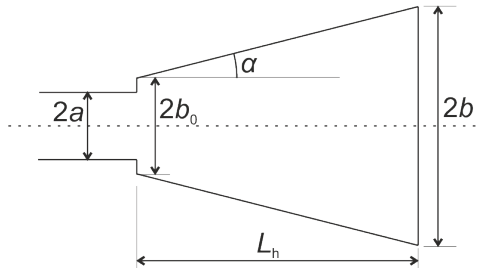


Figure 26: Picket-Potter horn arrangement.

The phase difference between the step transition and the aperture is given as [20]

$$\Delta\phi = 2\pi \int \frac{dz}{\lambda_{g\text{TE}}} - \int \frac{dz}{\lambda_{g\text{TM}}} \tag{51}$$

where $z$ is an axial distance along the horn, $\lambda_{g\text{TE}}$ a guide wavelength of the TE mode and $\lambda_{g\text{TM}}$ a guide wavelength of the TM mode.

The electric field at the aperture becomes with use of this horn more homogeneous, as depicted in Fig. 24, the simulated electric field distributon of the opened waveguide and the of the designed Picket-Potter horn shows Fig. 27.
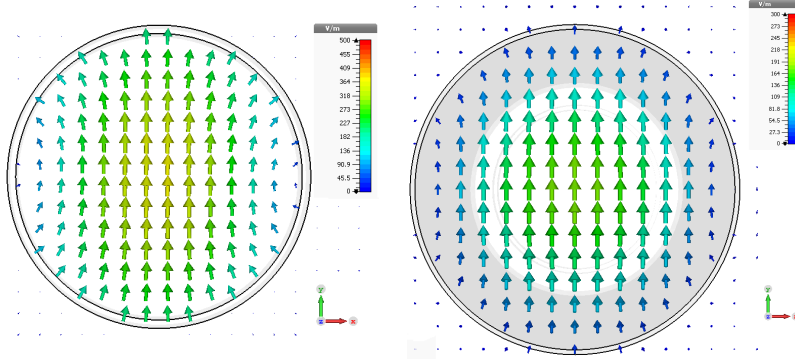


Figure 27: Electric field distribution at the aperture of the a) open-end waveguide, b) Picket-Potter horn.

For next design we will use Pickett-Potter horn, because of its easier arrangement and detailed analysises available in the literature. The exact dimensioning of the dual-mode horns needs to be done empirically. The basic condition for the correct function of this horn is widening of the waveguide section to the radius, which allow to propagate this $\text{TM}_{11}$ mode, but it is smaller than radius needed for propagation of the next $\text{TE}_{12}$ mode. These values are given at the 3 GHz by

$$a_{\text{TM}_{11}} = \tfrac{3.832}{2\pi f_d \sqrt{\mu\epsilon}}\,\text{m} \doteq 0.0609\,\text{m} = 6.09\,\text{cm}$$

$$a_{\text{TE}_{12}} = \tfrac{5.331}{2\pi f_d \sqrt{\mu\epsilon}}\,\text{m} \doteq 0.0848\,\text{m} = 8.48\,\text{cm} \tag{52}$$

The original design by Pickett [20] proposed a horn with a length $L = 10.62\lambda_0$ and another analyses in [25] or [21] propose a horn with a length of $L = 13.54\lambda_0$ and $L = 9.62\lambda_0$, respectively. These lengths are too long for our design at $f_d = 3$ GHz, because of limitation for the manufacturing with a 3D printer to maximal dimension of 20 cm.

Shorter realizations are presented in [27] and the following contribution [26], where series of design curves were produced for optimal input radius, aperture radius and horn length. The input radius of the horn considered in [27] are $b_0 = 0.65\lambda$ and $b_0 = 0.68\lambda$ and the corresponding optimal dimensions shows Fig. 28.
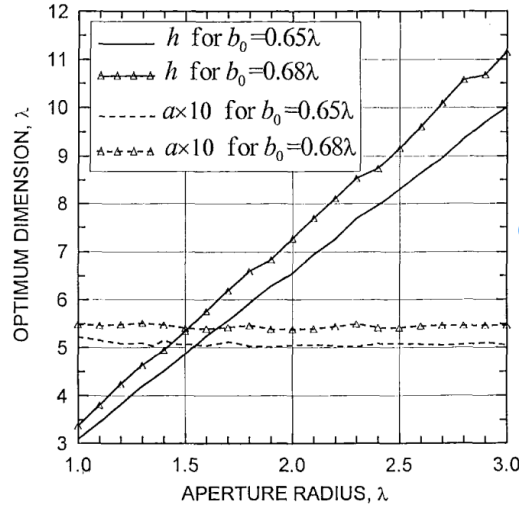


Figure 28: Optimal horn paramters, taken from [27].

In the own design we will design an optimal horn with as small length as possible.

# 8    3D print

For the manufacturing of the polarizer we will use a 3D printing method, also known as additive manufacturing. The early 3D printing printers were developed in 1980's, since the first filed patent were the patent of Dr Kodama in Japan in 1980 and the method was firstly called Rapid Prototyping technology. This early method was based on the liquid photopolymer, which was hardened by the UV laser at demanded sections. Because of difficulties of the new technology, the first commercial system started to sell up to in 1988 and the price for such system was very high and affordable for large companies, which could take advantage od fast prototyping of the new parts, e.g. in the automotive or any other product design. Through the 1990's and early 2000's a lot of new technologies were introduced, including depositing of the moltened plastic material in the layers on the base. After year 2000, when some patents expired, the 3D printing become popular also in the hobbyist and consumer usage, when a project RepRap contributed for the popularization and development of the affordable 3D printers not only for the professionals, but for the general public.

One of the most popular is the project RepRap, which is a self-replicating manufacturing machine concept. It is an open-source project and started a revolution in the 3D printing, because of the very big advantage of these printers, that the plastic parts for building RepRap printer can be printed by another printer and so only the metal parts and electronic needs to be bought. The design of these printers can be found on the Internet and is available to everyone. For people, who want to buy a completed printer, there are a lot of companies concerning with the 3D printers, which offers a huge variety of the printers with fully services.

The printing can be very time-consuming, according to the demanded quality of the printed object. The better quality required, the lower layers are deposited and thus the printing time is longer, for example a set of printed objects and the comparison of the printing quality can be be seen in Fig. 29.
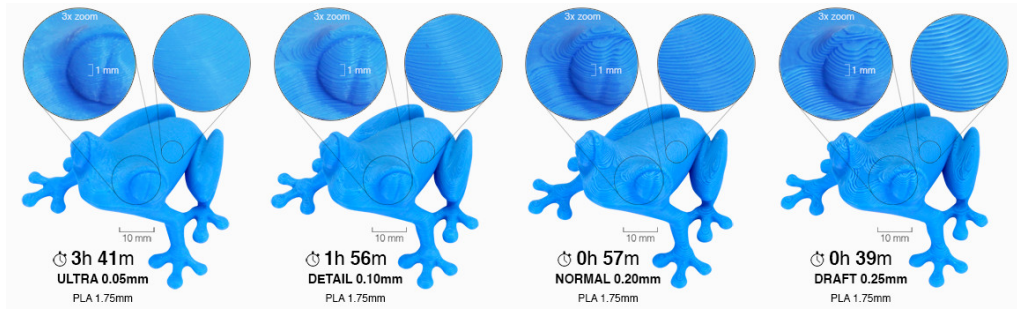


Figure 29: The comparison of printing time, the quality of the printed item and manufacturing time of Prusa i3 Plus 3D printer, taken from [29].

One of the most commonly used 3D printers for home amateur printing is a Prusa 3D printer. This printer is available at the Department of Electromagnetical Field at the Faculty of Electrical Engineering, polarizers designed during this thesis will be printed there.

## 8.1 Prusa 3D

Prusa 3D is a 3D printer model, which was launched by Josef Průša. This Czech 3D printer workes on the RepRap project since 2009 and since them he made one of the most well known 3D printing machines. The actual model is called Original Prusa i3 Plus 3D Printer, whose form and appereance can be seen in Fig. 30. This printer can print product to up to $200 \times 200 \times 200$ mm. It is characterized by the open frame structure, integrated LCD for use without a computer and easy printing setup. The printing nozzle has a diameter of 0.4 mm and it supports the printing filaments with a 1.75 mm diameter. The height of the printed layer is from 0.05 mm.



Figure 30: Prusa i3 Plus 3D printer, taken from [29].

## 8.2 Printing materials

For 3D printing there is a huge variety of printing materials, which differ in the characteristics, like brittleness, appearance after the printing or in the characteristic manufacturing attributes like different temperatures when being printed or need of the heated pad. The most often used materials for printing are thermoplastics, thanks to their advantage properties, but also other special materials like wooden or metal materials or conductive materials are available for uncommon use. The printing filaments are usually available with diameters 1.75 or 3 mm and they are sold in 0.5 or 1 kg rolls.

Thermoplastic is a plastic material, which becomes soft and melts above a temperature specific for the used material, whereas this temperature is for commonly used plastics in the temperature range from 100°C to 150°C. The heating process of the thermoplastics can be described by the glass transition temperature $T_g$ and the melting point $T_m$. Below the glass transition temperature $T_g$, the thermoplastic is usually fully crystallized and its structure is hard and brittle. Above the temperature $T_g$ and below the melting point $T_m$

the physical properties of a thermoplastic change dramatically, particularly the Young's modulus. Above the melting temperature $T_m$ the thermoplastic melts, whereas after cooling down it hardens, thus this temperature interval is used for printing. For this quality, thermoplastics are for its easy manufacturing widely used in the industrial manufacturing with processing methods like blowing, extrusion, injection moulding or welding. Most commonly used thermoplastics for the 3D printing is ABS, PLA, PET or HIPS. Usually they are available in wide variety of colours for creative designing.

**ABS (Acrylonitrile Butadiene Styrene)** is a commonly used 3D printer material, versatile for many applications and suitable for making durable parts that need to resist higher temperatures. For exemple LEGO cubes are made of ABS. Its glass transition temperature is $T_g \doteq 102°$ and hence it is amorphous, it has not true melting point. Standard printing temperature for ABS is about 230°C and when printed use a heated printed surface is recommended, as ABS will contract when cooled to warped part. During the printing ABS a toxic gas is generated, therefore a printing in a well ventilated room is necessary and breathing the fumes is not recommended. The ABS material can be smoothed to have a shiny surface using acetone.

**PLA (Polylactic Acid)** is near the ABS commonly used 3D printing material. It is biodegradable, made of corn or maize starch, and due to the lower printing temperature (180-220°C) it is one of the most eco-friendly materials available. It is dimensionally stable with low warping and any heated pad needs to be used for printing. PLA is an ideal material for home 3D printers like Prusa.

**PET (Polyethylene Terephthalate)** is a very strong material, it warps very little and has great thermal resistance.

**HIPS (High Impact Polystyrene)** is a very strong material, similar to the ABS, but it is dissolvable in Lemonen, so it can be use as a support material for complex shapes and then to be removed by dissolving.

Besides these standard printing filaments other special materials are available on the market, like filaments with a portion of carbon for high-stiffness parts, wood, bamboo or sand for natural look or filaments with metal parts, which can be smoothed after printing to have a realistic metal effect.

The main properties of the usual thermoplastics [30] used for 3D printing shows Tab. 3.

| **Material** | $T_p$ [°C] | **Price [\$/kg]** | **Advantage** |
|:---:|:---:|:---:|:---:|
| ABS | 220-235 | 28 | smoothable |
| PLA | 180-220 | 28 | warping-free |
| PET | 210-255 | 36 | thermal resistance |
| HIPS | 220-230 | 36 | dissolvable |

Table 3: Comparison of thermoplastics materials.

For the printing of the model designed in this thesis an ABS material with a diameter 1.75 mm, because of its durability, good shape stability and ability to be smoothed.

# 9 Metallizing of the printed parts

The printed models are made of the ABS, a thermoplastic polymer, that is not conductive. For the antenna design, the parts need to be metallized with conductive material. The metallizing of the plastic parts is a slightly complicated process, hence an electroplating, which requires conductive surface of the part for coating, can not be used in its simple way. Therefore another technique has to be chosen. In this theses metallizing with different techniques were used- vacuum metallizing process, highly conductive copper spray and aluminium spray.

## 9.1 Vacuum metallizing

Vacuum metallizing, called also vacuum coating, is a process for depositing of materials, mostly metals like aluminium, silver, gold or special alloys, etc. on the manufactured items, but also very specific layers used in optics can be used. The process take place in the vacuum chamber, whereas heating the coating material to its boiling point cause an evaporating of the material and letting them to condensate and deposit at the substrate material, which is intended for the metallizing. This technique is often used for metallizing of the plastics parts for the automotive industry, like for the lightning systems or for chromium plating of parts, which should have glaring shine. Since the deposited metal layer can be very homogeneous, vacuum metallizing can be used also for a very precious layering e.g. of the mirrors.

The process take place in the vacuum chamber, which is described in Fig. 31, wherein a vacuum level of $10^{-4}$ to $10^{-6}$ Pa has to be created, because of the straight-line trajectory of the evaporated particles and the mean free path as longest as possible. The metal for metallizing is then put into the evaporater, which is made of the metal or alloy, which does not evaporate at the evaporation temperature of the metallizing material and they are usually made of hard metals like Wo, Mo or Ta. The metallizing material is heated up to its evaporation temperature (usually 1000-2000°C), usually by the current flow through the metal or by the electron gun, whereas the electron beam is controlled by the magnet and is directed to the metal for evaporation.
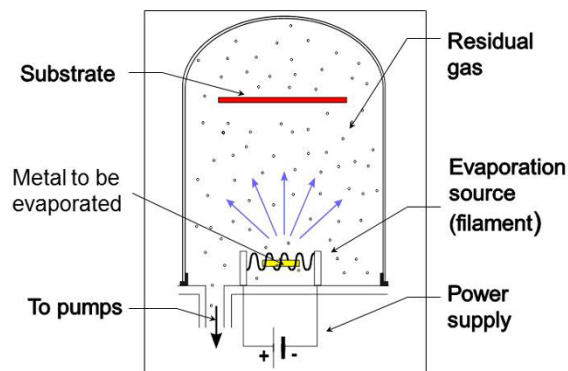


Figure 31: The arrangement of the vacuum chamber for coating, taken from [31].

## 9.2 Conductive sprays

As an alternative metallizing a highly conductive spray, called EMILAC, will be used. EMILAC contains a copper particles, that are for better conductivity coated with silver. This highly conductive, protective coating is to be used for shielding from the electromagnetic waves, it ensures protection both from electromagnetic interferences (EMI) and from electrostatic discharges (ESD). It does not attack the materials in common use and dryes quickly. The surface resistance of this spray, according to its technical data sheet [32], is lower than 0.5 $\Omega/mm^2$ at 0.25 $\mu$m film thickness and the attenuation for electromagnetic waves is 50-70 dB for 50 $\mu$m film thickness.

The second spray used during this project was aluminium spray Prisma Color with high content of the pure aluminium.

Figure 32: For metallizing a EMILAC conductive copper spray was used, taken from [32]
.

# 10   Design of the antenna

Because of limitation of the 3D printing technique, which can not allows printing complex arrangements with septum or irises, a polarizer in a waveguide with such perturbation elements will be designed, that can be easily printed using the 3D printer.

At the output of the polarizer a Pickett-Potter horn will be completed to apply dual-mode radiating for more symmetric radiation pattern and lower side lobe level. The design will go out of independent design of the polarizer with the feeding probe in the circular waveguide structure and of the dual-mode horn. To feed this antenna, a coaxial feed line with an input impedance of 50 $\Omega$ will be used.

For compact design of the antenna and because of limited printing area of the 3D printer, the transition section from the coaxial feeding to the circular waveguide and the polarizer section section will be designed being integral. The arrangement of the designed antenna is shown in the Fig. 33.
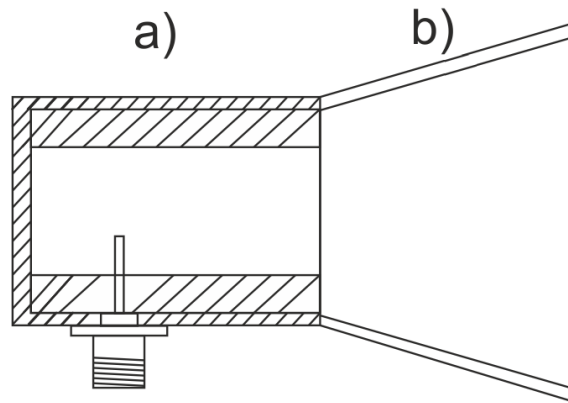


Figure 33: Compact design of the polarizer with a) the waveguide section with a coaxial feeding and a polarizing section and b) a dual-mode horn.

All modelling and simulations were done using the Computer Simulated Technology (CST) Studio Suite software.

## 10.1  Polarizer in circular structure

The first design will be situated in the circular waveguide structure with conductive plate at the opposite sides of the waveguide and these plate will be rotated at 45° to excite two orthogonal modes.

### 10.1.1  Waveguide structure

The main waveguide structure will be made of a circular waveguide with such a diameter that enables mode $TE_{11}$ to propagate at the design frequency $f_d$=3 GHz, but the next modes has to be cut off. Because of the axial symetry of the next modes, the next mode that could be excited with the probe showed below, will be the $TM_{11}$ mode. Since the waveguide radius has to allow to propagate the $TE_{11}$ mode and not yet excite the $TM_{11}$, the constant, derived from the Bessel's functions $p'_{11}$ for TE mode and $p_{11}$ for TM mode, needs to lie in the interval $1.841 < p_{11}(p'_{11}) < 3.832$. Using the Formulas 53 and 54 we get the required radius of the waveguide

$$a_{TE_{11}} = \frac{1.841}{2\pi f_d \sqrt{\mu\epsilon}}\, \mathrm{m} \doteq 0.0293\,\mathrm{m} = 2.93\,\mathrm{cm} \tag{53}$$

$$a_{TM_{11}} = \frac{3.832}{2\pi f_d \sqrt{\mu\epsilon}}\, \mathrm{m} \doteq 0.0609\,\mathrm{m} = 6.09\,\mathrm{cm} \tag{54}$$

For first design a radius $a$=4 cm was chosen.

### 10.1.2  Coaxial line to circular waveguide transition

Since the antenna is usually be feeded with the coaxial line, a section transiting the TEM mode of the coaxial line to the TE mode of the circular waveguide must be designed. For this purpose we will consider the simplest coaxial transition in the form of electrical coupling, that is made with extension of the center conductor into the waveguide for creating of cylindrical probe, that excites the dominant $TE_{11}$ mode. At the end of the waveguide, behind the probe, a short circuit locates in a distance $D$, called backshort. For the basic adjustment $\frac{\lambda_g}{4}$ for backshort distance and $\frac{\lambda_0}{4}$ for the probe length are usually used, but these dimensions need to be adjusted in the impedance matching analysis. The arrangement of the transition section is show in fig. 34.

The coaxial connection is designed as a SMA connector having an 50 Ω impedance. The dimensions for modelling we get from the equation for the characteristic impedance of the coaxial line [10] as in Fig. 35

$$Z = \frac{Z_0}{2\pi\sqrt{\epsilon_r}} \ln \frac{b}{a} \tag{55}$$

where $Z_0$ is an impedance of the free space ($\sqrt{\frac{\mu_0}{\epsilon_0}}$), $\epsilon_r$ is a electric permittivity of used dielectric of the $b$ is a diameter of the outer conductor and $a$ is a diameter of the inner conductor. The inner pin of the SMA connector has a diameter $a$=1.27 mm, the dielectric
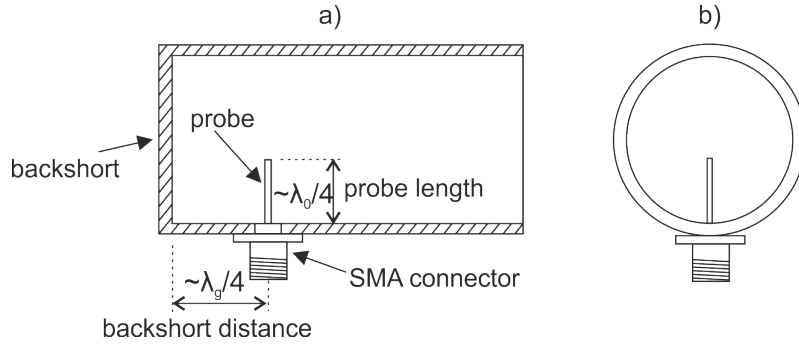
Figure 34: Longitudinal (a) and cross section (b) of the coaxial to the circular waveguide transition.

is a PTFE with $\epsilon_r$=2.1 and so from the Equation 55 we get the outer diameter $b$=4.25 mm.
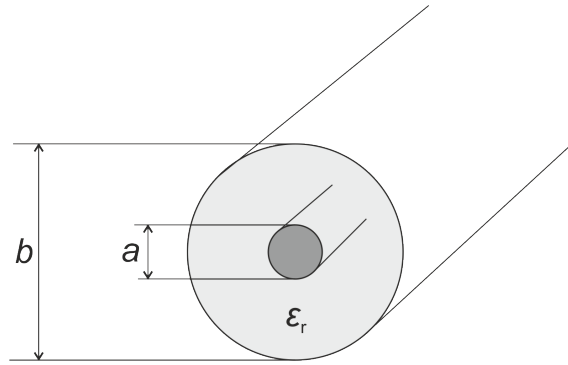


Figure 35: Coaxial line cross-section.

The arrangement of the modelled connector is shown in the Fig. 36, the blue material inside is a PTFE, which is a dielectric material.
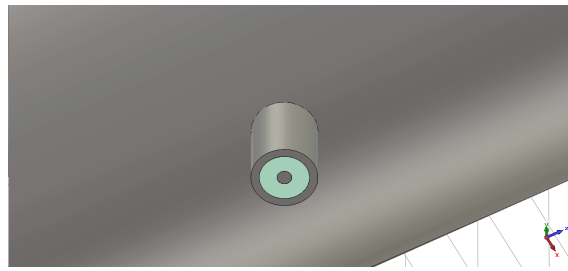


Figure 36: Detail of the modelled SMA connector.

There is a combination of probe radius, probe length and backshort distance what transform the impedance of the waveguide to a desired 50 $\Omega$ of the coaxial line. All these factors can be used for optimising of the impedance matching. The optimal distance is usually kept around 0.25 $\lambda_g$, what is given by the constructive interference of the incident and reflected waves in the probe plane.

According the equation 44 for $\lambda_g$, this optimal distance $d_{\mathrm{opt}}$ can be evaluated as

$$d_{\text{opt}} = \frac{2\pi}{\sqrt{\left(\frac{2\pi f}{c}\right)^2 - \left(\frac{1.841}{0.04}\right)^2}} \, \text{m} \doteq 3.67 \, \text{cm} \tag{56}$$

The optimalization of the parameters were done and the starting and optimized values shows Tab. 4. After optimizing the reflection coefficient is lower than -40 dB. The transition is quite narrowband, as can be seen in Fig. 37, what results from the resonant character of this kind of transition with placing the probe in the particular distance from the backshort. For better wideband characteristics a shaped probe could be used.

| Parameter | Proposal | After optimization |
| --- | --- | --- |
| Waveguide radius | 40 mm | 38 mm |
| Probe length | 25 mm | 23 mm |
| Backshort distance | 36.7 mm | 36 mm |
| Reflection coef. $S_{11}$ at 3 GHz | -7.45 dB | -40.5 dB |

Table 4: Starting parameters for the coaxial to the circular waveguide transition.
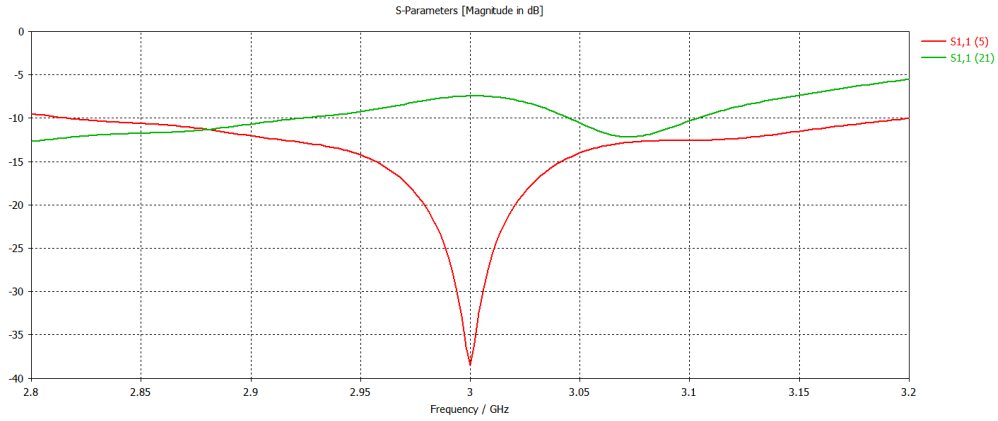


Figure 37: Reflection coefficient $S_{11}$ of the designed transition with starting (green) and optimalized parameters (red).

Hence these values are valid for unperturbed waveguide, in the waveguide with flats the wavelength $\lambda_g$ is different and the backshort dimensions need to be adjusted for best impedance matching.

### 10.1.3 Polarizing section

The polarizing section will be made in the shape of two flat structures, which reduce the diameter of the waveguide in the symmetrical manner on the opposite walls of the waveguide as can be seen in Fig. 38. These slabs need to be rotated 45° relative to the feeding port to excite two orthogonal modes.
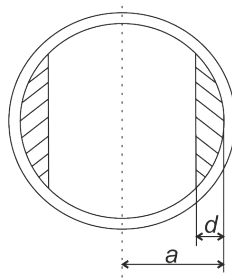


Figure 38: Cross-section of the designed polarized in the circular waveguide

The $TE_{11}$ will split in the waveguide with pertrubations into two orthogonal modes, which will be described here as parallel and perpendicular components with respect to the flats direction, as in Fig. 39.
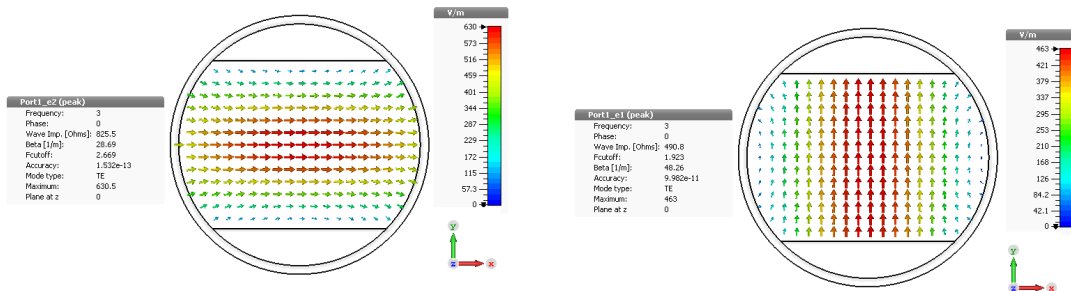


Figure 39: Two orthogonal modes in the circular waveguide a) parallel and b) perpendicular to flats

An analysis will be done to find the right dimensional proportion of the polarizer radius $a$ without perturbations and the depth $d$ of the slabs. We will consider a radius $a = 3.8$ cm as the polarizer radius designed in Section 10.1.1 and the depth of the flats will be changed from 0 to 16 mm.

Fig. 40 shows a dependence of the wavelength $\lambda_g$ of the orthogonal modes in relation to the proportion of depth $d$ of the perturbation flats and radius $a$ of the waveguide without perturbations. From the graph can be seen, that for any penetration ($a/d$=0) the wavelengths of both modes is the same, hence the situation corresponds with an empty waveguide, which is symmetric. When the flats becomes greater, the symmetry is being disrupted and the difference between the both modes is getting more perceptible, whereas the wavelength of the parallel increases rapidly, while the wavelength of the perpendicular mode decreases slowly. This difference between the wavelengths of the both modes will be essential for creating the required phase shift as described below. There is a limitation as the plate depth should not restrict the feeding probe due to the geometrical arrangement at 45° in the waveguide.
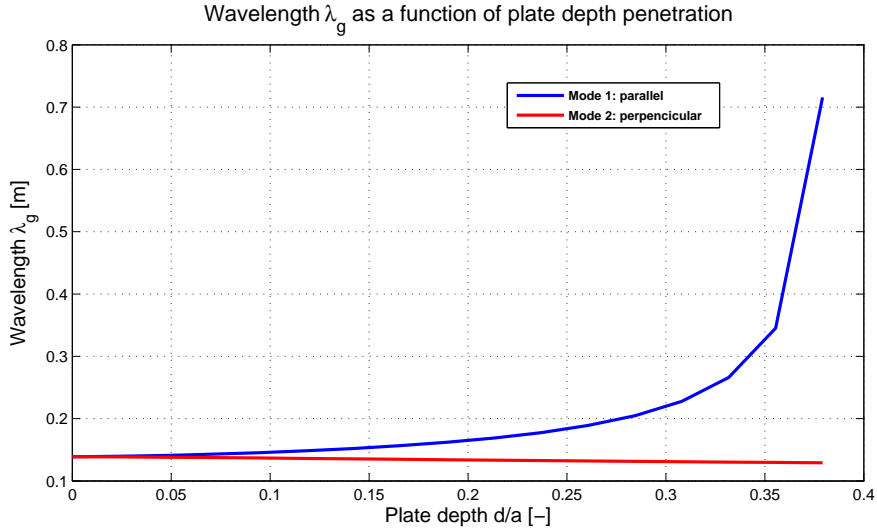
Figure 40: Wavelength $\lambda_g$ as a function of plate depth $d/a$

The plate depth influence the cutoff frequency of the structure, because of changed dimension. Fig. 41.
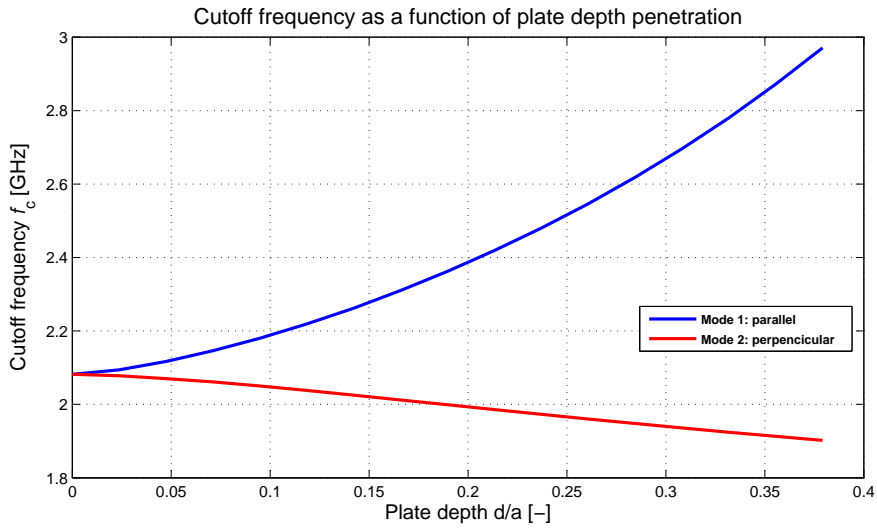


Figure 41: Cutoff frequency $f_c$ as a function of plate depth $d/a$

Since the dimensions of the waveguide cavity are changing, both modes also have different cutoff frequencies, when the cutoff frequency of the parallel mode is growing more rapidly than the of perpencicular component. With higher $d/a$ ratio, the cutoff frequency of parallel mode can be to close to the design frequency $f_d$= 3 GHz, what is not desirable and could cause, that this mode will not be propagate.

For our design, the length of the polarizer should be as small as possible, due to restrictions of the 3D printer described in Section 8 and also for building a polarizer with a compact size. Therefore the phase constant difference should be as high as possible to shorten the polarizer length. In our design will consider about 10% margin of the cutoff frequency from the design frequency $f_d$, due to the higher bandwidth possibility and significant attenuation

constant close behind the cutoff frequency as described in 5. This condition is fulfilled for about 8 mm flat depth, what corresponds to the phase constants $\beta_1$= 28.69 rad/m for the parallel mode and $\beta_2$=48.26 rad/m for the perpendicular mode. The desired polarizer length for a phase shift 90° or $\frac{\pi}{2}$ needs to fulfill the condition

$$(\beta_2 - \beta_1)l = \frac{\pi}{2} \tag{57}$$

which implies the length $l$ of the polarizer to be

$$l = \frac{\pi}{2\Delta\beta} = \frac{\pi}{2*(48.26 - 28.69)} \doteq 8.03\,\text{cm} \tag{58}$$

The first proposal for the dimensions of the polarizer are then: inner radius of the waveguide section $a$= 38 mm, length of the waveguide $L$= 80.3 mm, the depth of the flats $d$= 8 mm. With these parameters a model was build, which was then carefully analysed.

Since there is a more parameters, that can influence the behaviour of the antenna, they have been analysed separately and described below. The characteristics we will monitor are an reflection coefficient $S_{11}$ and the axial ratio $AR$. The main parameters in our design are length of the polarizer $L$, position of the feeding probe from the backshort $z_{\text{feed}}$ and probe length $L_{\text{probe}}$. We will now analyse these parameters step by step.

Another analysed parameter was a distance from the backshort $z_{feed}$, which was changed in the interval from 20 mm to 50 mm. The Fig. 42 and 43 shows the frequency dependence of the $S_{11}$ and $AR$. It is obvious, that this parameter will have a significant influence on the reflection coefficient, because of the interference of the incoming wave and the wave reflected from the backshort, they should arrive in phase for right impedance matching.
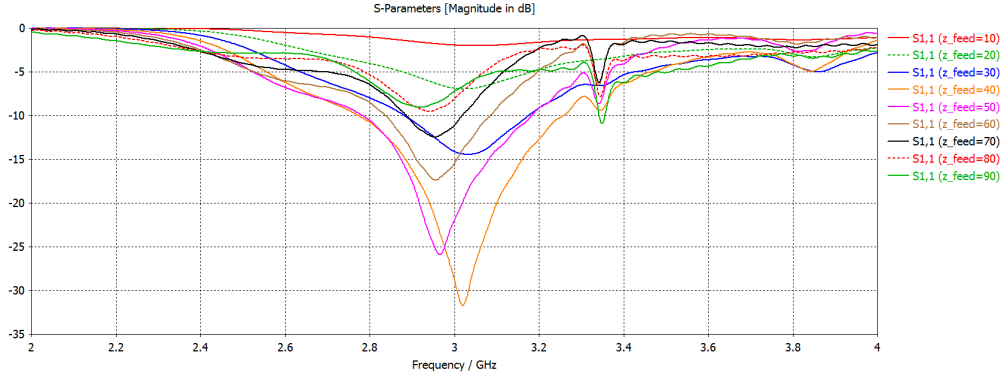


Figure 42: Backshort length influence on the reflection coefficient $S_{11}$
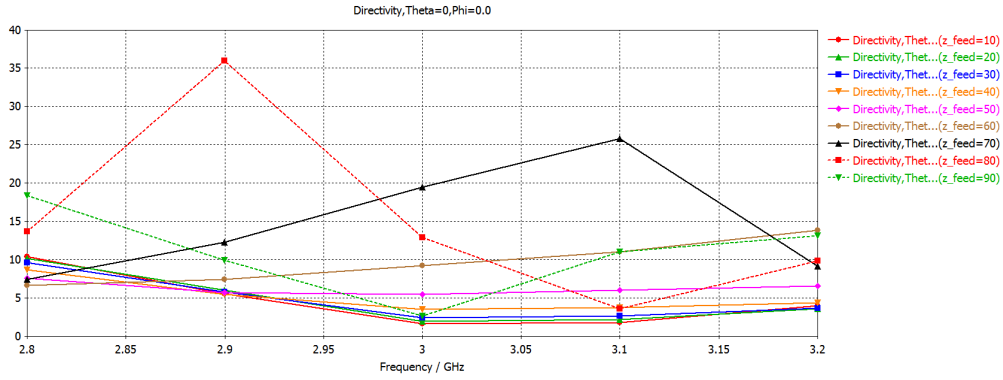
Figure 43: Backshort length influence on the axial ratio $AR$

Next analysed parameter was a length of the polarizing section. The length of the polarizer gives the appropriate phase shifting of the both modes in the structure, the changing of the length should thus change primarily the AR, but consequently reflection coefficient due to the another field distribution in the waveguide. Now, the probe distance will be constant $d=$ 60 mm, according to the best impedance match from Fig. 42 and the polarizer length will be changed from 70 mm to 150 mm.
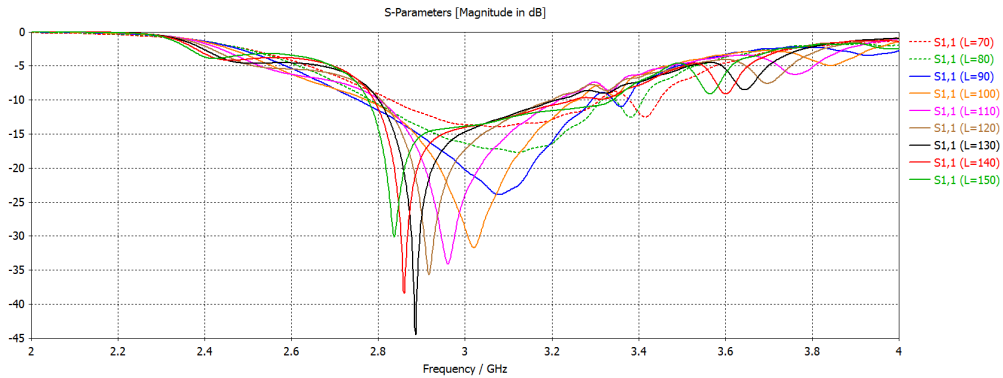


Figure 44: The effect of the polarizer length on the $S_{11}$.
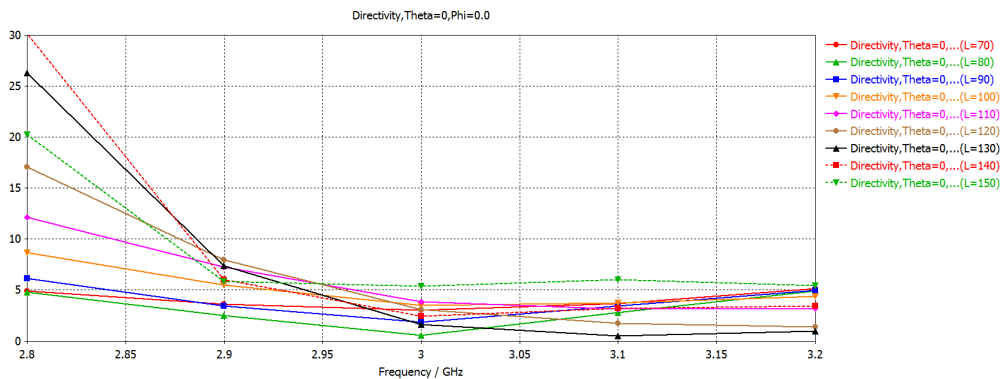


Figure 45: The effect of the polarizer length on the $AR$.

The probe length $L_{probe}$ has been changed from 20 mm to 35 mm. The probe forms here an monopole over ground plane, which resonates at a frequency given by the condition

$\frac{\lambda_0}{4}$. The change of this parameter should thus change the resonant frequency and so the impedance matching, while the axial ration should remain, since it given mainly by the polarizing section. Fig. 46 shows the frequency behaviour of the axial ratio. It can be seen very little influence on the axial ratio, on the other hand the reflection coefficient vary with the changing probe length, as in Fig. 47.
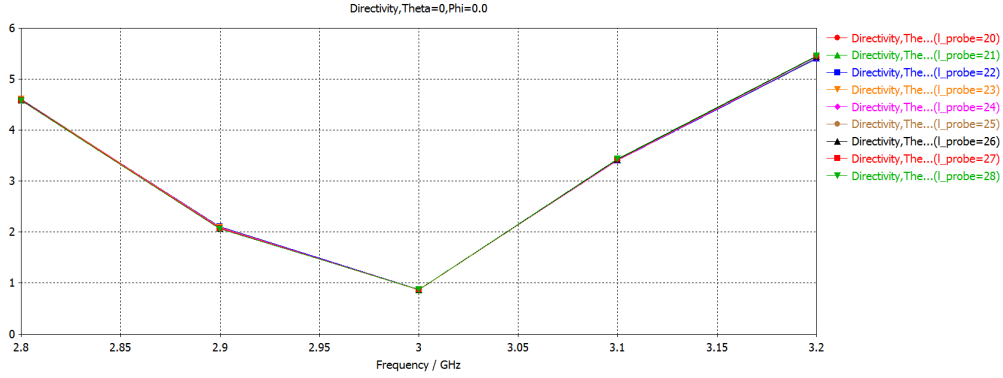


Figure 46: Probe length influence on the axial ratio AR
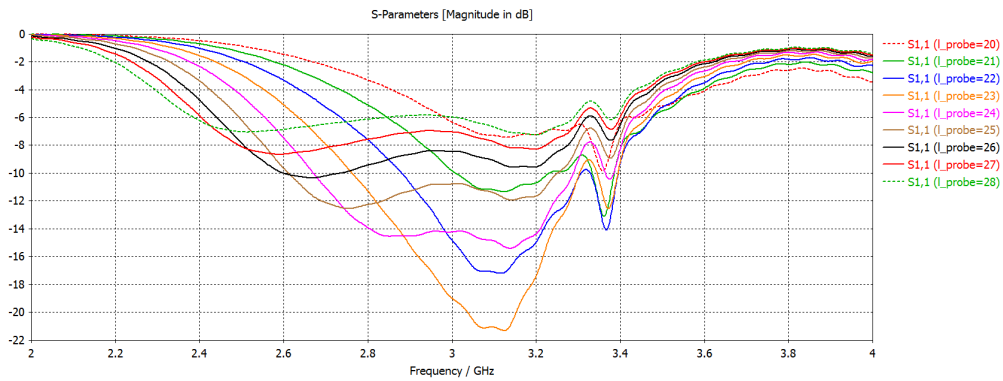


Figure 47: Probe length influence on the reflection coefficient $S_{11}$

The final dimensions were optimized to achieve the best axial ratio parameter and the final form of the polarizer can be seen in Fig. 48.
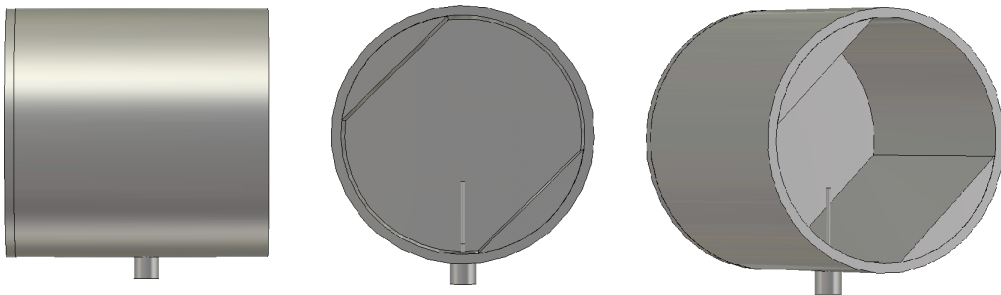


Figure 48: The model of the designed polarizer in the circular waveguide.

The corresponding axial ratio and radiating pattern show Fig. 49 and 50.
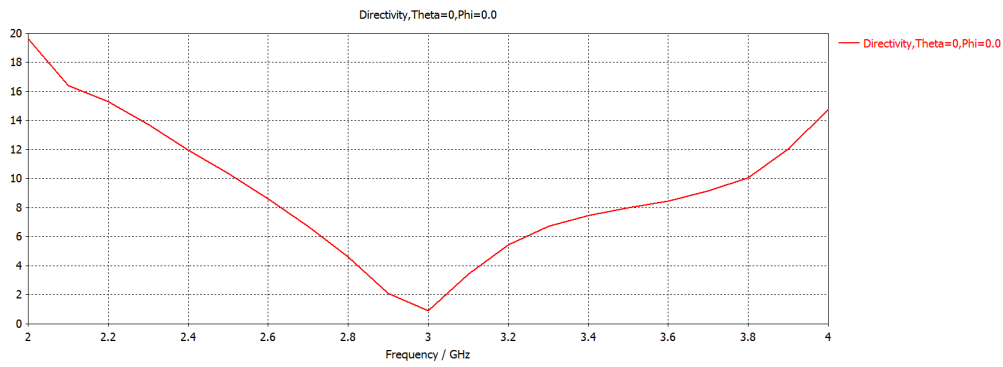
Figure 49: Frequency dependence of the axial ratio of the circular polarizer.
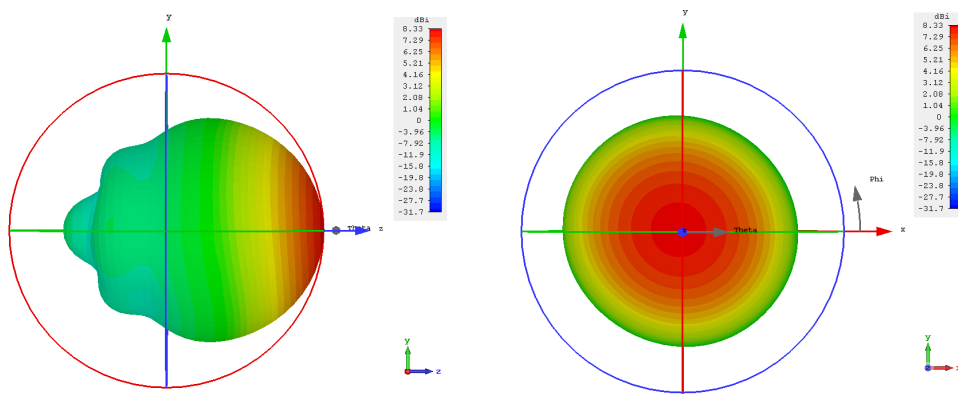


Figure 50: Radiation patterns of the designed circular polarizer in the side and front view

For better impedance matching and wider bandwidth usually a probe with larger radius can be used, what should improve the impedance matching. Because of availability of probe with a radius 1.9 mm, an simulation of this probe was done. The result can be seen in Fig. 51, while the axial ratio changes only little, as in Fig. 52. Here an wider probe will not be used, because of worse impedance matching at $f_d$=3 GHz.
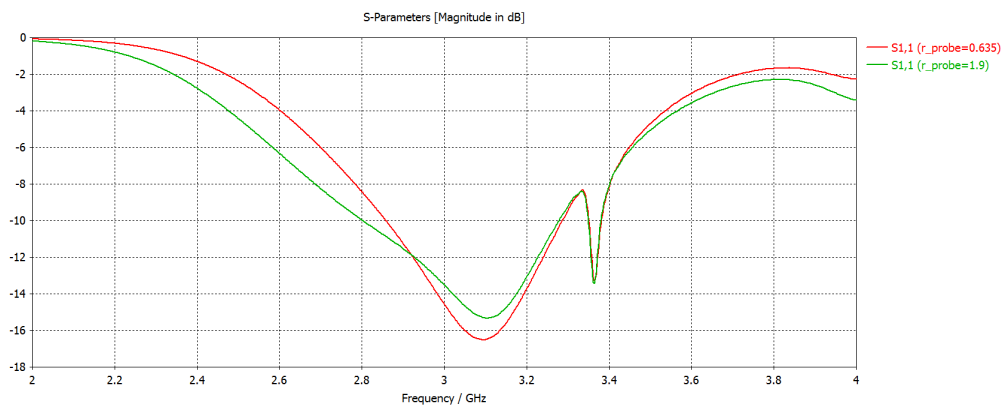


Figure 51: The probe width influence on reflection coefficient $S_{11}$.
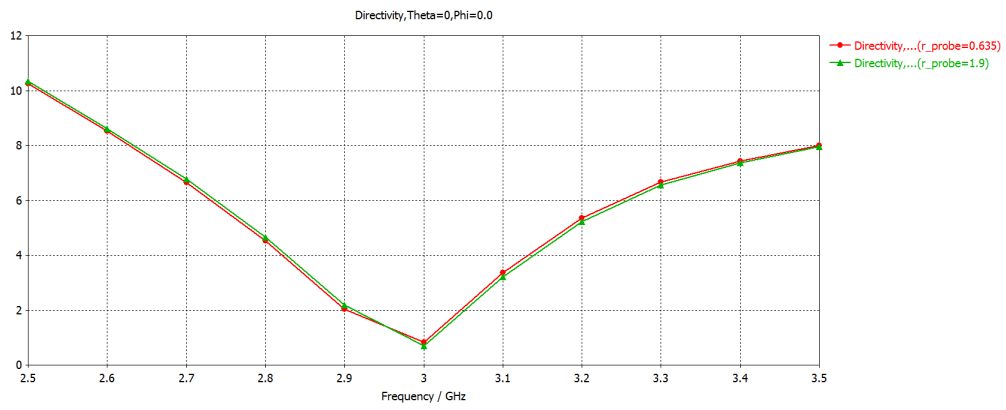
Figure 52: The probe width influence on the axial ratio of the circular polarizer.

### 10.1.4 Pickett-Potter horn

Using the above relations in Section 7.2 and simulation in CST Studio Suite an optimal horn was designed. The parameter of this horn shows Tab. 5 and the corresponding model shows Fig.53.

| Parameter | Dimension [$\lambda_0$] | Dimension [mm] |
|---|---|---|
| Input waveguide radius | 0.51 | 51 |
| Input horn radius | 0.65 | 65 |
| Aperture radius | 1 | 100 |
| Horn length | 3.05 | 305 |

Table 5: Optimal parameters for the Pickett-Potter horn design
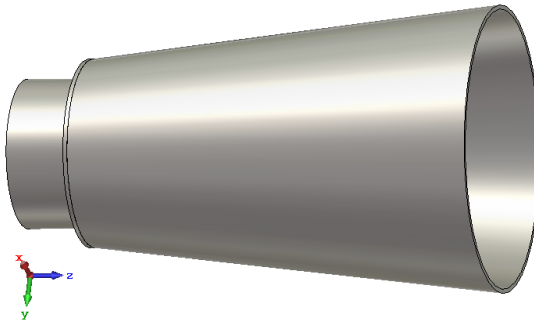


Figure 53: The model of the optimal Picket-Potter horn of length 3.05 $\lambda_0$
.

The directivity of this Pickett-Potter horn shows a directivity of 14.6 dBi and the side lobes are suppressed very effectively and their level is -40.5 dB. The radiating pattern show Fig. 54 and Fig. 55.
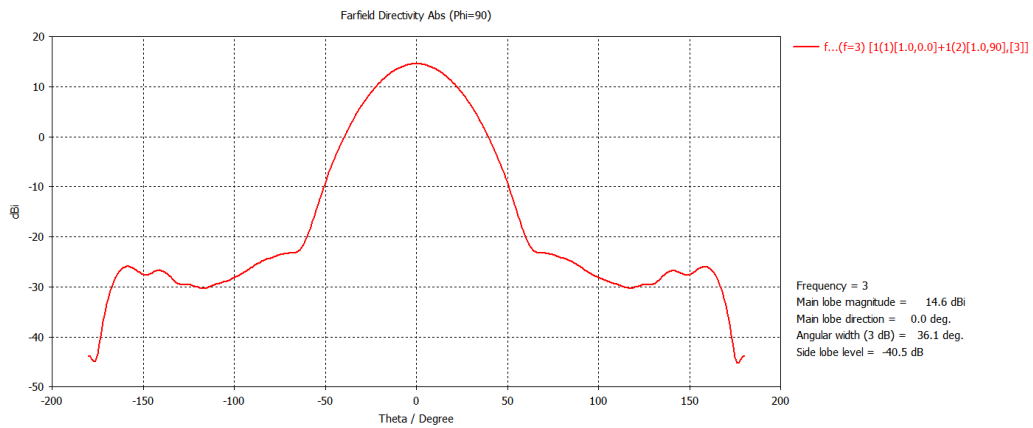


Figure 54: Directivity of the optimal Picket-Potter horn.

| Type | Farfield |
| Approximation | enabled (kR >> 1) |
| Monitor | farfield (f=3) [1(1)[1.0,0.0]+1(2)[1.0,90],[3]] |
| Component | Abs |
| Output | Directivity |
| Frequency | 3 |
| Rad. effic. | -0.01784 dB |
| Tot. effic. | -0.03212 dB |
| Dir. | 14.58 dBi |

Figure 55: Radiation pattern of the optimal Picket-Potter horn.

Because of the complex structure, there are any analytical solutions available, the design of the Pickett-Potter horn needs to be done empirically and the length of the horn needs to be shortened to maximal 200 mm.

Unfortunately, it has shown, that the shortening of the horn, which would be needed for printing, leads to worse results. The parameters of the optimized horn of the length 190 mm shows Tab. 6.

| Parameter | Dimension [mm] |
| --- | --- |
| Input waveguide radius | 51 |
| Input horn radius | 65 |
| Aperture radius | 76 |
| Horn length | 190 |

Table 6: Optimized parameters of the designed Pickett-Potter horn

Fig. 56 shows a radiating pattern of the designed Pickett-Potter horn. It can be seen good symmetry of the horn is achieved and that the side-lobes (-20.2 dB) are not suppressed ideally as with the optimal Pickett-Potter horn (-40.5 dB), designed in Section 7.2. Also the directivity of this horn is lower due to the shortening of the horn. Because of the limited size, sufficient parameters can not be achieved and it was decided not to print this limited horn for measurement.
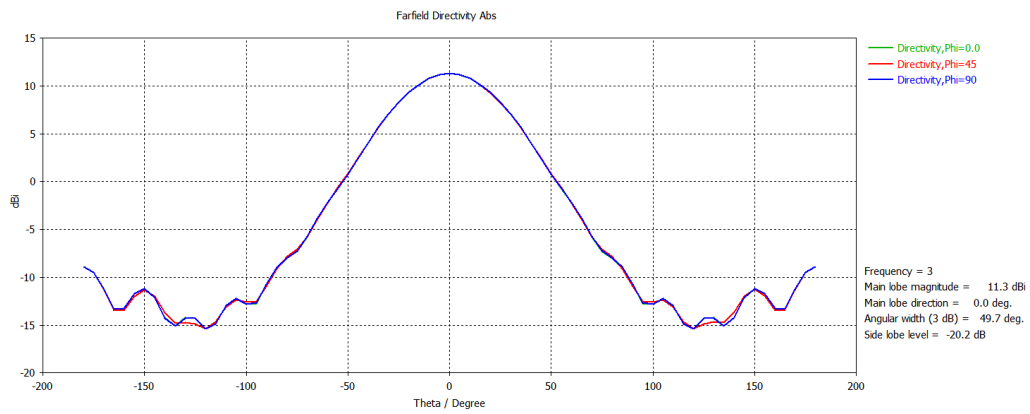
Figure 56: Directivity characteristics of the designed Pickett-Potter horn

The final model of the shortened Picket-Potter horn shows Fig. 57.
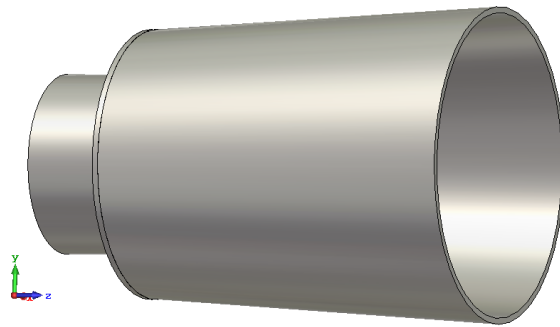


Figure 57: The designed model of the Pickett-Potter horn

### 10.1.5   Final design of the circular polarizer

The optimized dimensions of this polarizer shows Tab. 7.

| Parameter | Dimension [mm] |
|---|---|
| Waveguide radius | 38 |
| Length | 83 |
| Plate depth | 8 |
| Probe radius | 0.635 |
| Probe length | 23 |
| Backshort distance | 43 |
| Wall thickness | 3 |

Table 7: Optimized parameters of the polarizer in the circular waveguide.

The reflection coefficient of the designed polarizer is -19 dB at the design frequency $f_d$=3 GHz. The polarizer is impedance matched with -15 dB in the interval from 2.9 to 3.2 GHz.
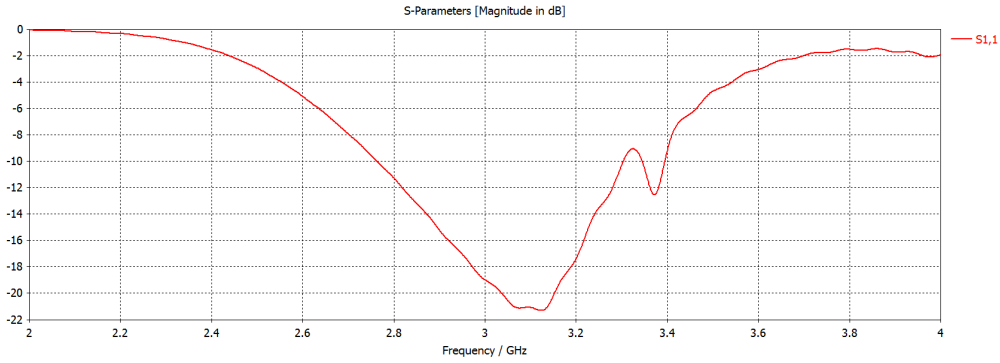


Figure 58: The impedance matching of developed circular polarizer.

The axial ratio better than 3 dB is achieved in the interval from 2.86 GHz to 3.08 GHz, as in Fig. 59. In this sense the polarizer is very narrowband.
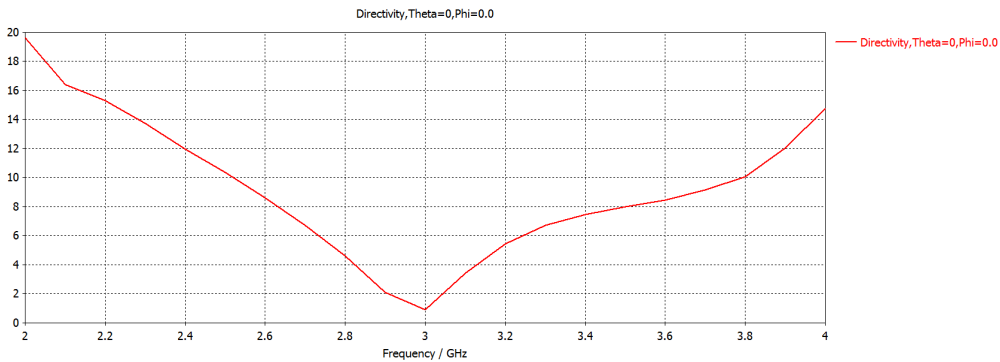


Figure 59: The AR of developed circular polarizer as a function of frequency.

As can be see in Fig. 60 the axial ratio lower than 3 dB in the angle $\phi$ from -62 to 81°.
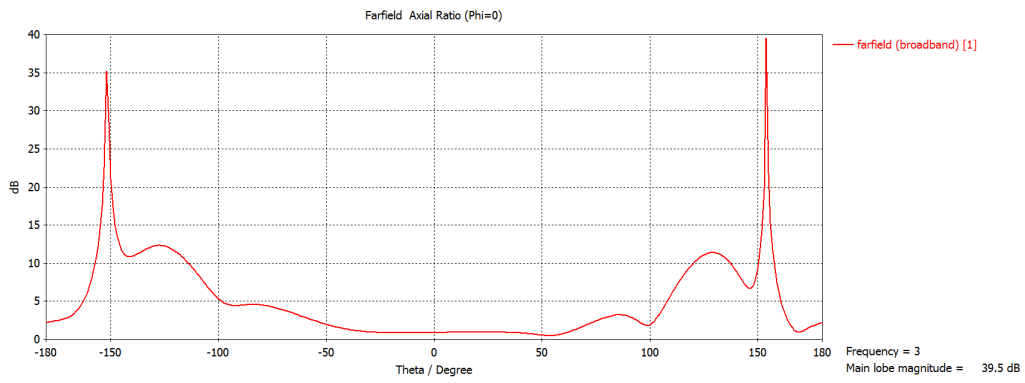
Figure 60: The angle distribution of the AR.

Fig. 61 shows the radiation pattern in the $\phi$=0, 45 and 90° planes and Fig. 62 in 3D. The field has a little asymmetry, which is primarily caused by the asymmetric feeding.
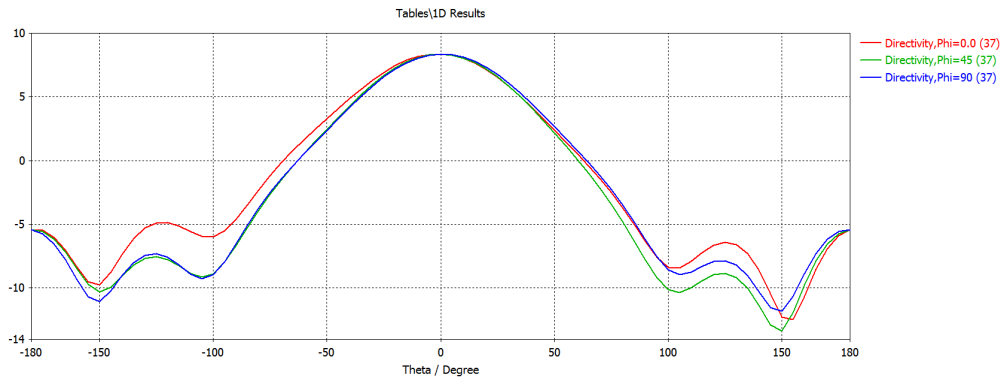


Figure 61: The radiating of the circular polarizer in the $\phi$=0, 45 and 90° planes.
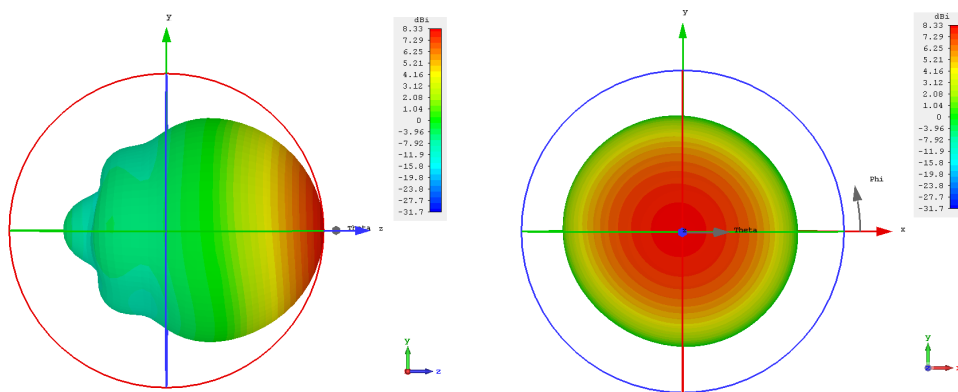


Figure 62: Radiating pattern of the designed circular polarizer in the side and front view.

Fig. 63 shows the electric field cuts in the planes z=0, 30, 43, 75 and 100 mm.



(a) $z$=0 mm, back side

(b) $z$=30 mm

(c) $z$=43 mm, feeding probe

(d) $z$=75 mm

(e) $z$=100 mm, outside the polarizer
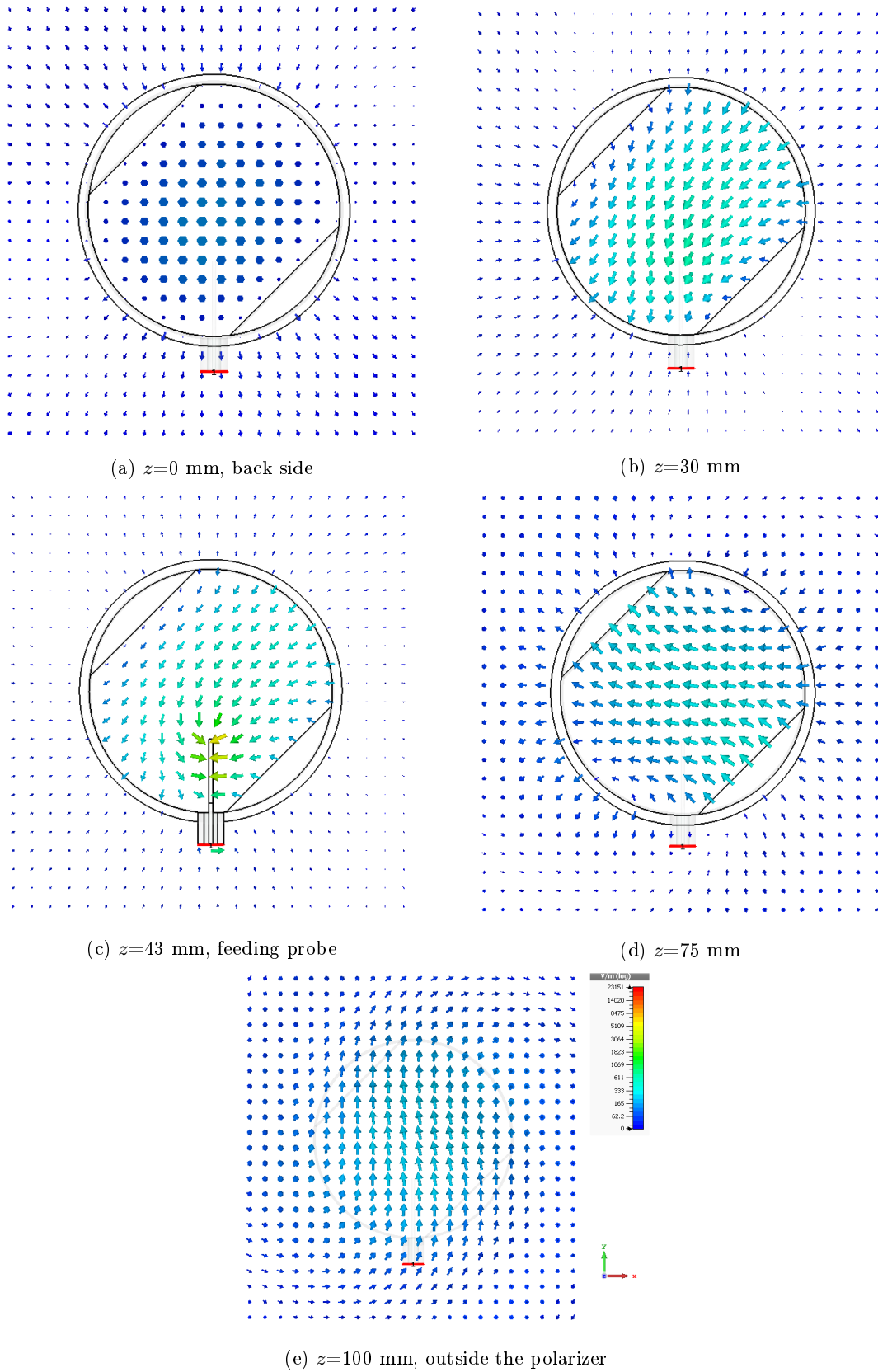
Figure 63: Electric field of the circular polarizer in planes $z$=0, 30, 43, 75 and 100 mm.

The cross-polarization suppression of this polarizer is 26.3 dB in the boresight direction as in Fig. 64.
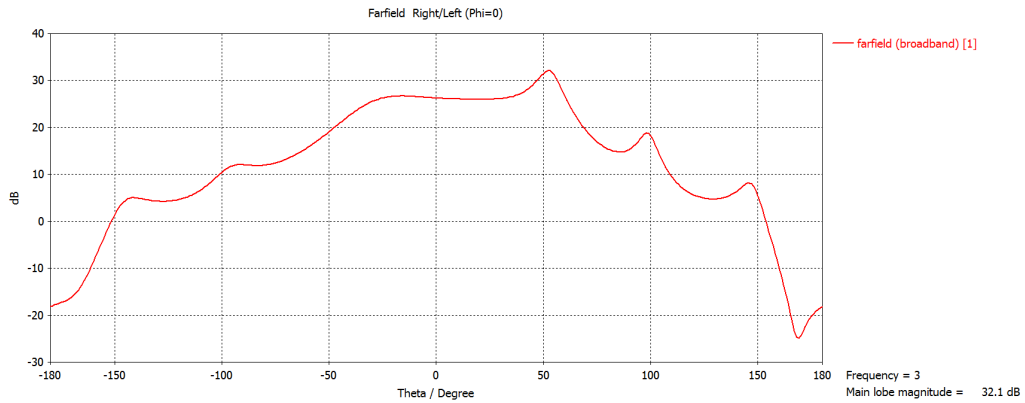


Figure 64: Cross-polarization suppression of the ciruclar polarizer.

After successful simulation, the model needs to be adjusted and prepared for the manufacturing. The probe is removed, auxiliary plate suitable for connector attachment surrounding the opening for the probe and a holder is created at the bottom for better attaching of the antenna during the measurement and the dimensions of the polarizer are adjusted for the metallizing by adding 0.5 mm to the radius and moving the hole for probe with 0.5 mm. The final model shows Fig. 65.
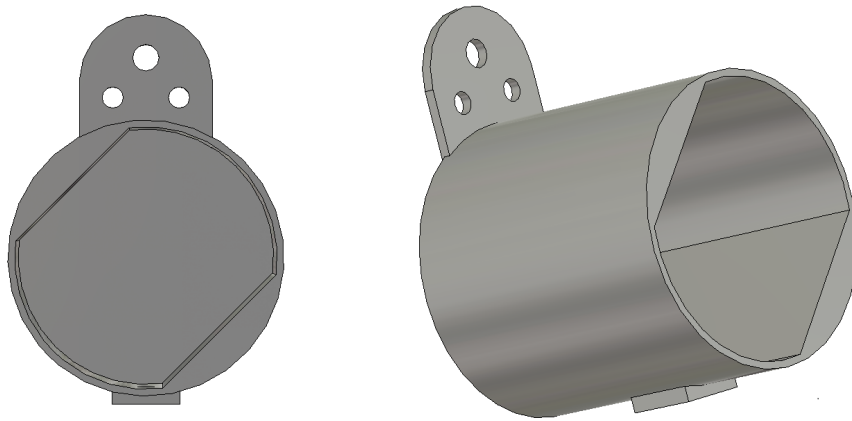


Figure 65: Final model of the circular polarizer ready to be printed in the top and side view.

As can be seen in Fig. 66, the phase of the radiated wave changes over the aperture and the antenna is circularly polarized.
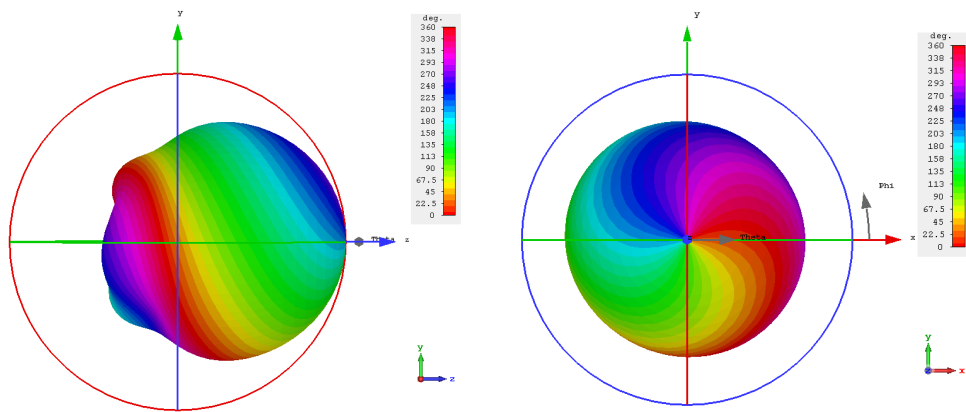


Figure 66: The phase pattern of the designed circular polarizer in the side and front view.

## 10.2 Elliptical polarizer

The design of the elliptical polarizer is very similar to the circular polarizer described above, thus the entire process will not be shown in details.

The simulated electric field distribution of two orthogonal modes in the elliptical waveguide shows Fig. 67.
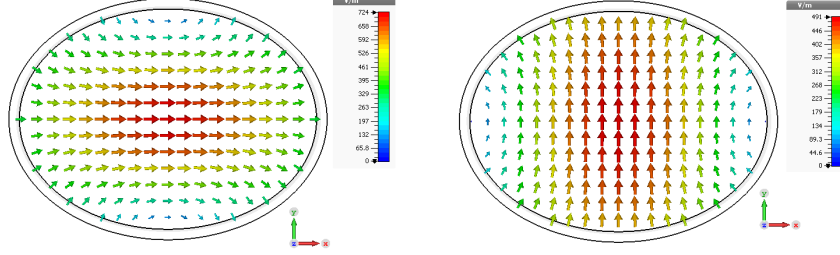


Figure 67: Two orthogonal modes in the elliptical waveguide a) parallel and b) perpendicular to the perturbation.

We will do an analysis similar to the performed for the circular waveguide in Section 10.1. We will study a relation of the perturbation, which can be described by the paramter $d$, meaning a shortening of the minor axis of the ellipse in relation to the circular cross section. The cross-section of elliptical waveguide shows Fig. 68.
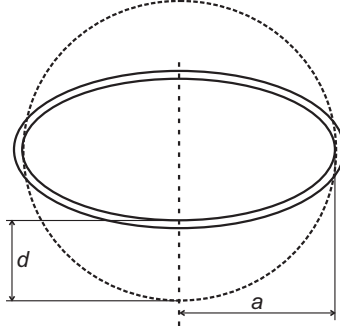


Figure 68: Elliptical waveguide arrangement.

As a starting shape of the elliptical polarizer was chosen circular waveguide with $R$=38 mm and the narrowing depth $d$ will be changed from 0 mm, what corresponds to the circular waveguide, to 12 mm.

As a first proposal the radius $r$=38 mm and shortening $d$=6 mm were used according to the above studies. From this values the length of the polarizing section should be

$$l = \frac{\pi}{2\Delta\beta} = \frac{\pi}{2*(39.71 - 26.37)} \doteq 11.8\,\text{cm} \tag{59}$$

This would be a case for only the polarizing section, the compact arrangement with the probe in the polarizing section will change this length.

In the basic arrangement, these parameters will be changed: backshort distance $d$, length of the polarizer $l$ and probe length $l$ and their effect on the reflection coefficient $S_{11}$ and axial ratio $AR$ will be analysed.
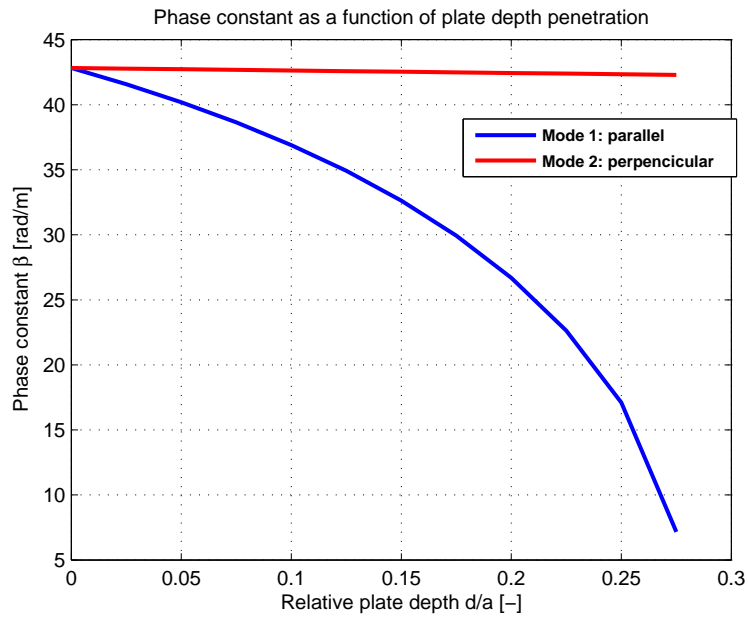
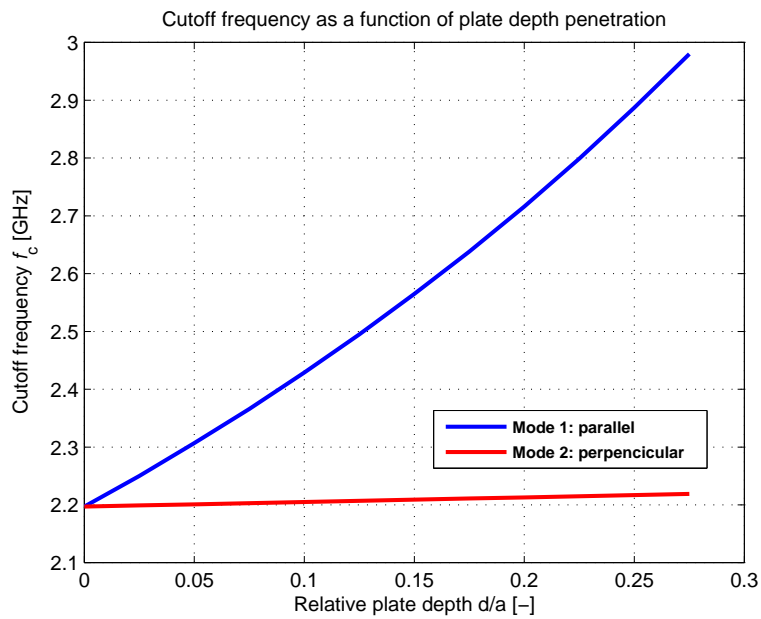Figure 69: Propagation constant $\beta$ as a function of shortening $d/a$



Figure 70: Cutoff frequency $f_c$ as a function of plate depth $d/a$.

The distance from the backshort $d$ will affect the reflection coefficient of the polarizer, as Fig. 71 shows, while the $AR$ will change much less as in Fig. 72. The probe distance is changed here from 10 mm to 90 mm.
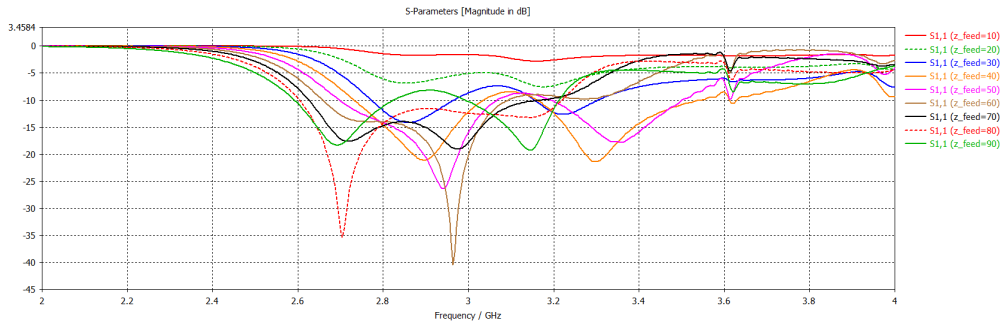
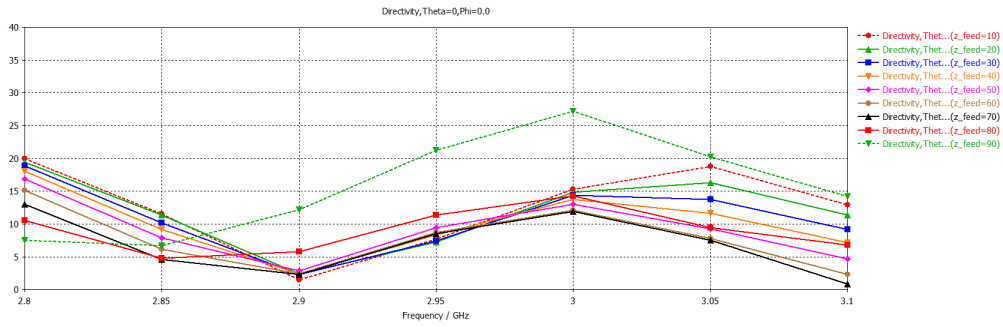Figure 71: The effect of the probe distance from the backshort on the $S_{11}$.



Figure 72: The effect of the probe distance from the backshort on the $AR$.

The length of the polarizer will affect both the impedance matching, because of the changed field distribution in the waveguide and the axial ratio, because of the different polarizing length. Now, the probe distance will be constant $d=$ 60 mm, according to the best impedance match from Fig. 71 and the polarizer length will be changed from 70 mm to 150 mm.
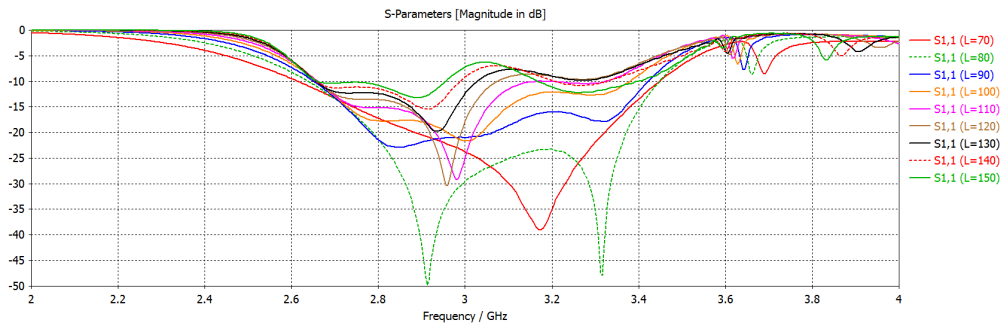


Figure 73: The effect of the polarizer length on the $S_{11}$.

57
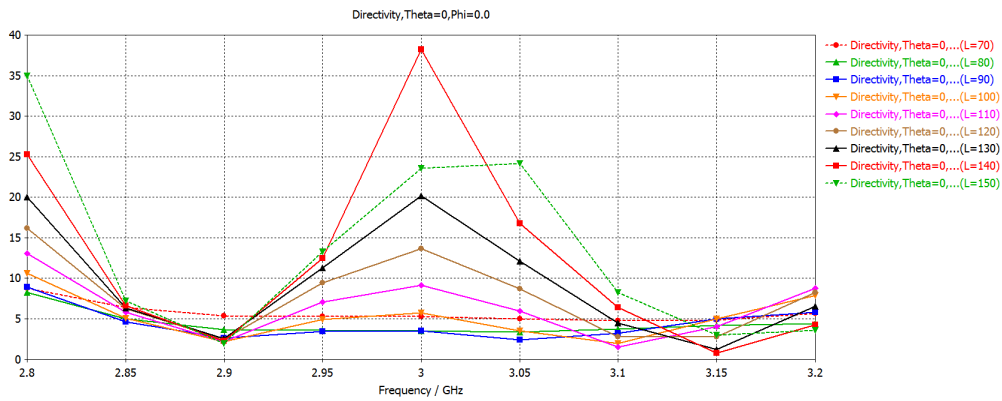
Figure 74: The effect of the polarizer length on the $AR$.

The probe length changes just the impedance matching, the $AR$ should change very less.
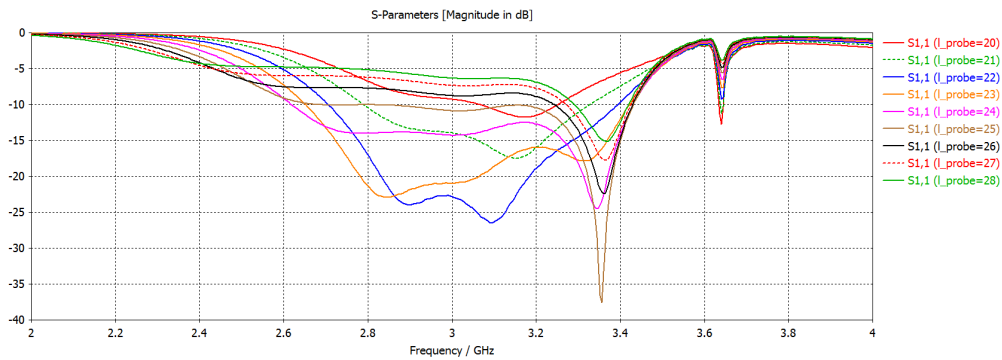


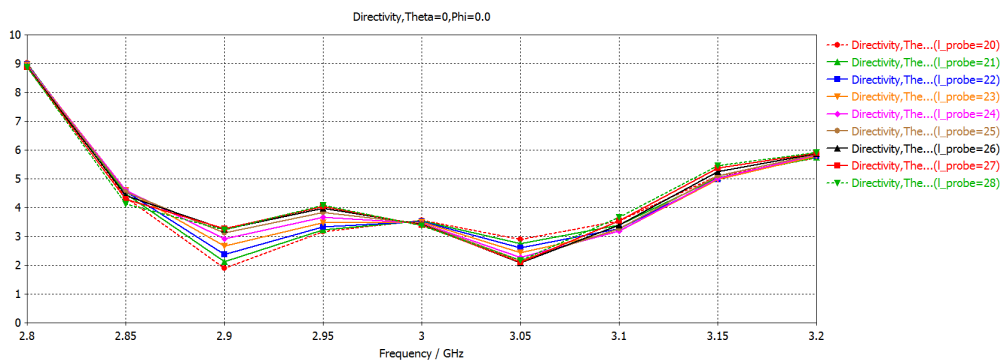Figure 75: The probe width influence on the $S_{11}$ of the elliptical polarizer.



Figure 76: The probe width influence on the $AR$ of the elliptical polarizer.

For better impedance matching and wider bandwidth a probe with larger radius can be used, what improves the impedance matching as in Fig. 77, while the axial ratio stays with no change. Instead of probe wide as the SMA inner pin with a radius 0.635 mm, a probe with a radius 1.9 mm will be used.
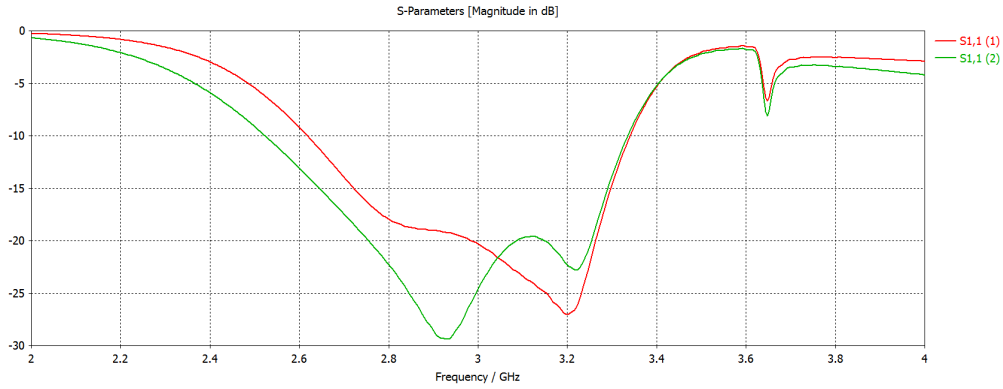
Figure 77: The wider probe improves the bandwidth of the polarizer.

The design is now finished and the final dimensions for the polarizer in the elliptical waveguide are shown in Table 8 and the model is shown in Fig. 78.

| Parameter | Dimension [mm] |
|---|---|
| Waveguide radius | 38 |
| Length | 88 |
| Plate depth | 6 |
| Probe radius | 1.9 |
| Backshort distance | 70 |

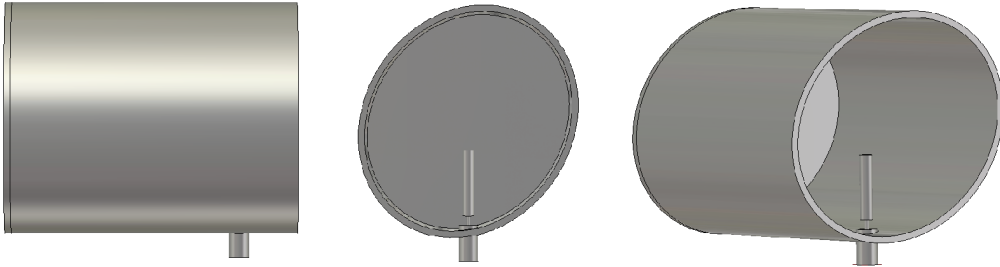Table 8: The final parameters of the polarizer in the elliptical waveguide



Figure 78: The model of the designed polarizer in the elliptical waveguide.

The reflection coefficient of the designed polarizer is -24.5 dB at the design frequency $f_d$=3 GHz. The polarizer is impedance matched with -15 dB in the interval from 2.65 to 3.3 GHz.

The axial ratio better than 3 dB is achieved in the interval from 2.86 GHz to 3.03 GHz, as in Fig. 80. In this sense the polarizer is very narrowband.

As can be seen in Fig. 81, the axial ratio at $f_d$= 3 GHz is lower than 3 dB in the angle $\phi$ from -55 to 55 degrees.
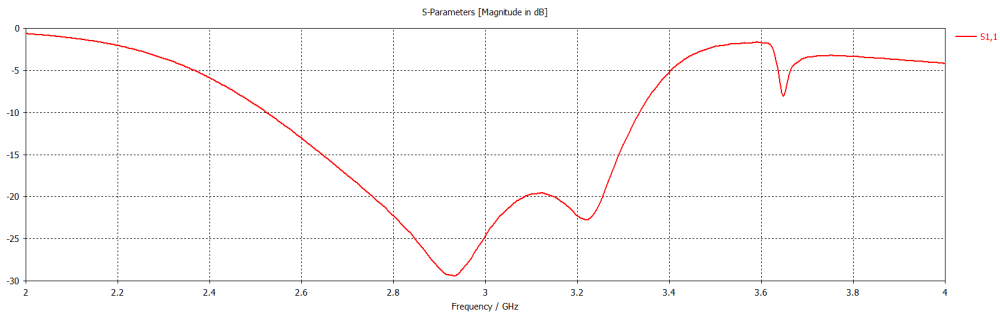
Figure 79: The impedance matching of developed elliptical polarizer.
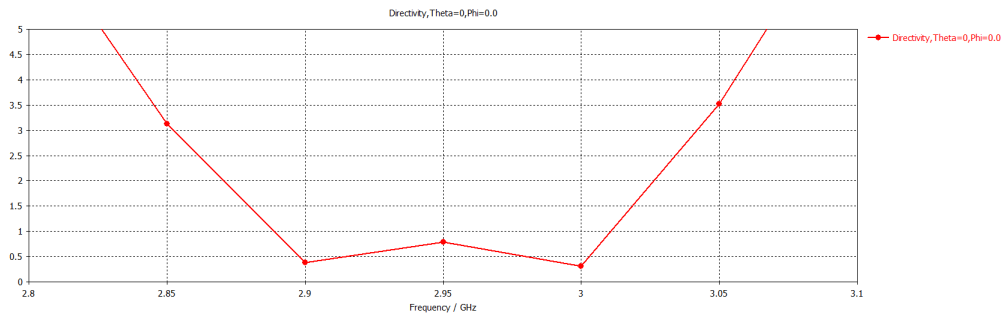


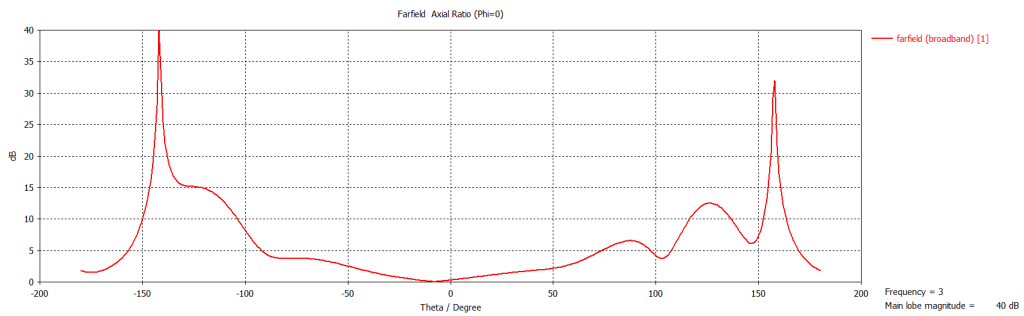Figure 80: Frequency dependence of the axial ratio of the elliptical polarizer.



Figure 81: The angle distribution of the AR.

The radiating pattern show Fig. 82 in the $\phi$=0, 45 and 90° planes and Fig. 83 in 3D.
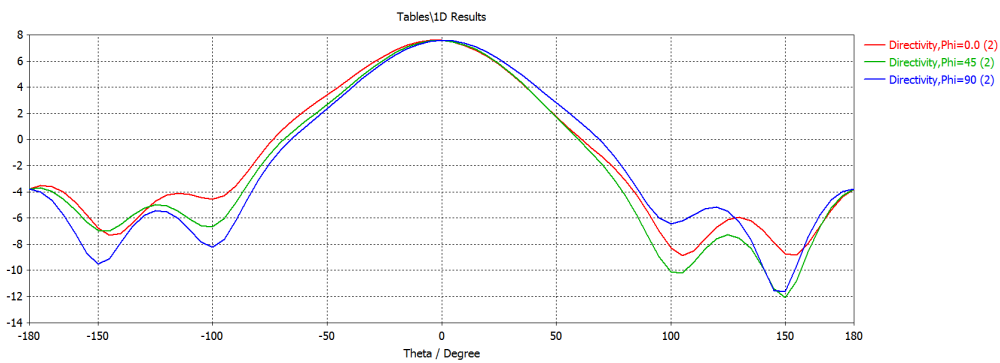


Figure 82: The radiating of the elliptical polarizer in the $\phi$=0, 45 and 90° planes.
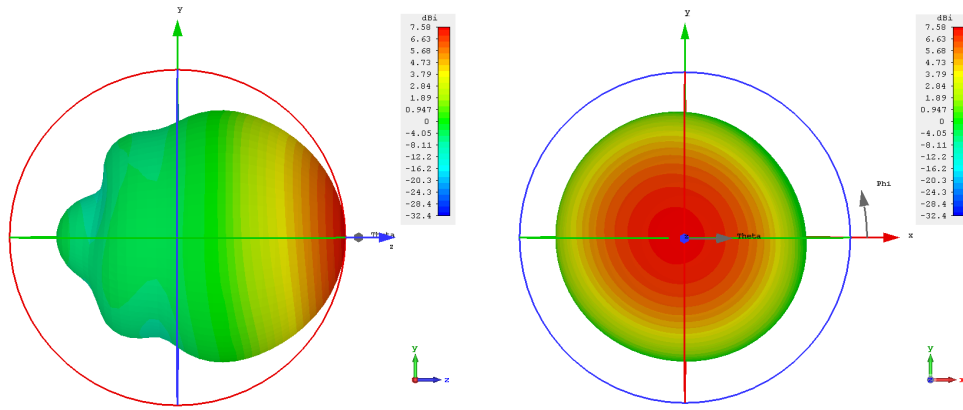
Figure 83: Radiation pattern of the designed elliptical polarizer in the side and front view.

As can be seen in Fig. 84, the phase of the radiated wave changes over the aperture and the antenna is circularly polarized.
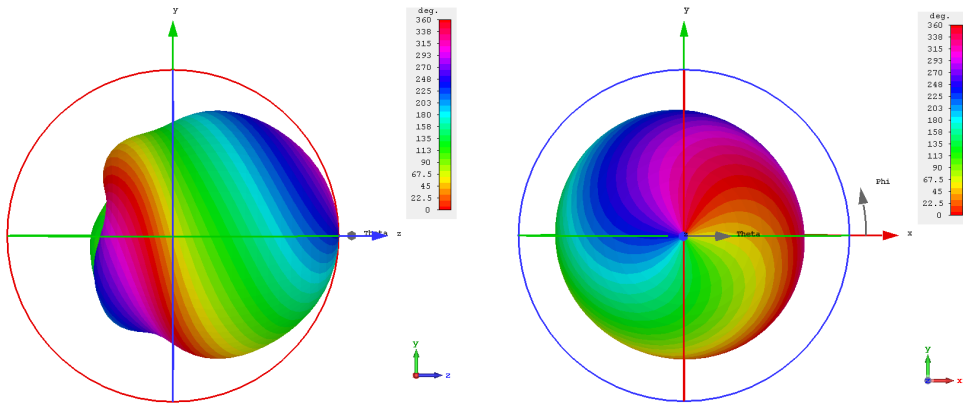


Figure 84: The phase pattern of the designed elliptical polarizer in the side and front view.

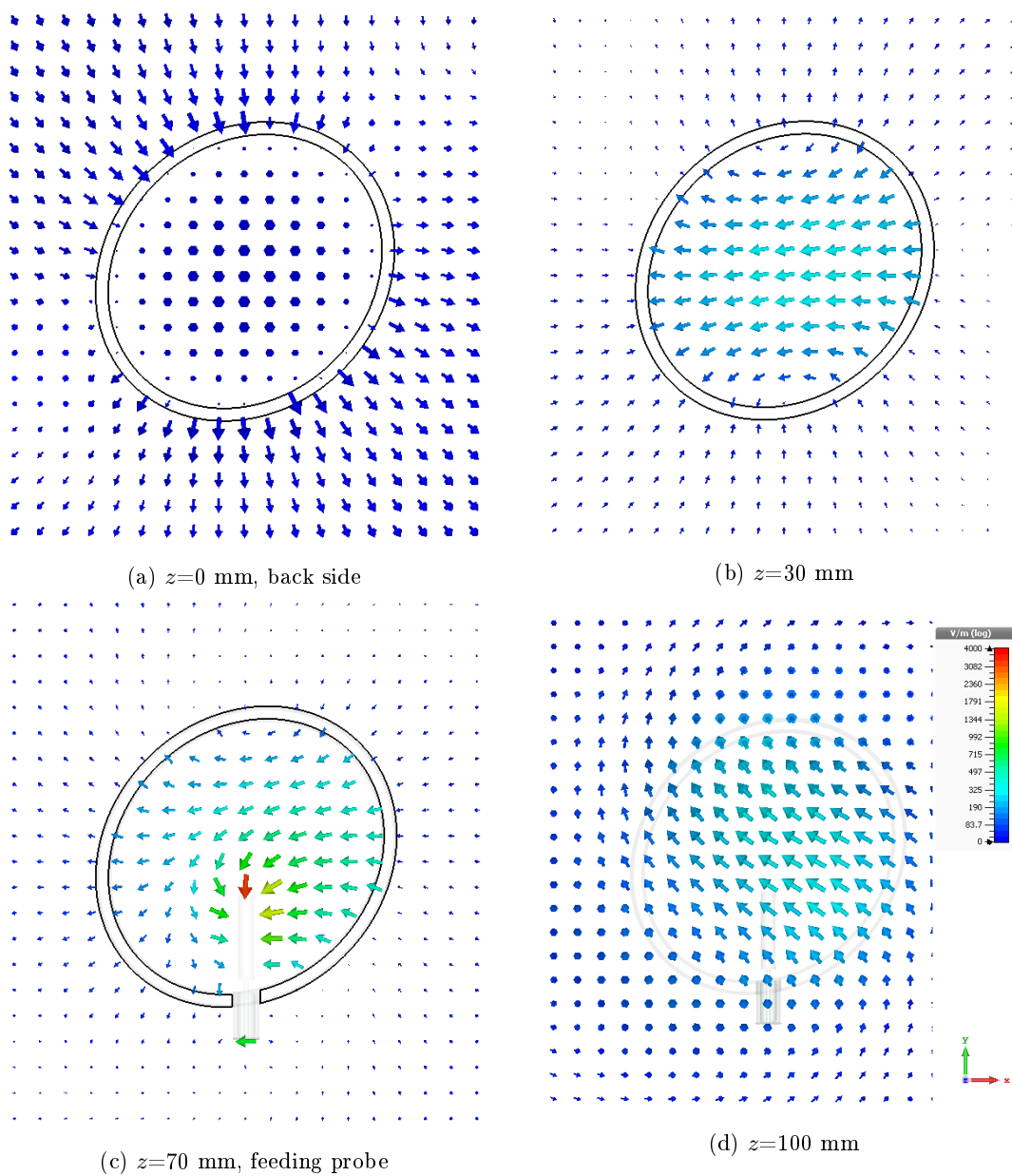Fig. 85 shows the electric field cuts of the elliptical polarizer in the planes z=0, 30, 70 and 100 mm.



(a) $z$=0 mm, back side

(b) $z$=30 mm

(c) $z$=70 mm, feeding probe

(d) $z$=100 mm

Figure 85: Electric field of the elliptical polarizer in planes $z$=0, 30, 70 and 100 mm.

# 11 Manufacturing of the polarizers

## 11.1 3D printing

After modelling and simulation of the antenna in the CST Studio The printing of the developed polarizer will be easily made by the 3D model exporting to the .stl format, which is directly supported by the Prusa 3D printer. The only changes needed for the model adjustment for the successful printing is removing of the SMA connector and enlarging of the model due to the metallizing with adding 0.5 mm to the total dimensions of the model.

After successful development of the models of the polarizers the models will be printed by the Prusa 3D printer and prepared for the measurement.

The printing time is a time-consuming process and the printer settings can influence noticeable the quality. For purpose of this thesis, the models were printed with the 1.75 mm filament with layer hight 0.25 mm and 25% filling of the full sections to save up material. The overall dimensions (without the holder) and printing durations of the designed models shows Tab. 9.

| Model | Dimensions [mm] | Filament [m] | Printing time [hours] |
|---|---|---|---|
| Circular | $81 \times 81 \times 86$ | 46.6 | 5:01 |
| Elliptical | $77 \times 67 \times 91$ | 27.4 | 3:22 |

Table 9: Printing times and filament consumption.

## 11.2 Metallizing

More companies engaging in the vacuum metallizing were approached, but unfortunately most of them can not execute metallizing of only few samples, because of a need to create a special holder for insertion of the items to be metallized in the vacuum chamber. The only company, which agreed to metallized was Zlín Precision s.r.o., which focuses on production of injected plastics parts mainly for the automotive industry and their subsequent surface finishing with an aluminium coating. Two models were metallized here, one circular and one elliptical. Despite of repeating of the metallizing process twice, the metallizing can not get to the bottom section and the metallized layer is therefore very thin. Because of this, onlyu the elliptical polarizer were leaved with just the vacuum metallized layer and the circular polarizer were spray with the aluminium sprey.

Another two models were metallized with the conductive copper spray, whereas three layers were applied.

## 11.3 Feeding assembly

The last part of the manufacturing process is attaching of the SMA connector with attached probe. The arrangement of the probe shows Fig. 86

Figure 86: The view of the attached connector with probe.

The whole manufacturing process is done, the polarizers are finished are ready for beeing measured. All the completed models are shown in Fig. 87 and 88.



Figure 87: Circular and elliptical polarizers with copper coating.



Figure 88: Circular polarizer with vacuum metallizing and elliptical polarizers with aluminium spray.

## 12 Measurement and comparison simulation and measurement

The measurement was done in the anechoic chamber at the Department of electromagnetical field. The following parameters were measured: impedance matching, radiation patterns, polarization patterns and gain.

For the measurement antenna RF Spin SCSA-27 was used. It is a logarithmic spiral antenna with with circular polarization, its gain is about 5 dBi at 3 GHz.

For the axial ration measurement a horn antenna RF Spin DRH20 was used. It is double ridged waveguide horn antenna and its gain is about 9 dBi at 3 GHz. Its aperture has dimensions $104 \times 78$ mm.

The antennas should be in the far field distance during the measurement. If we consider the aperture size of developed polarizers to be 80 mm and the maximal measuring frequency to be $f$=4 GHz, the far-field distances of measured and measuring antennas are according to the Equation 14 given by

$$d_{f\,\text{SCSA}-27} = \frac{2 * 0.11^2}{\lambda} = 0.32\text{m}$$

$$d_{f\,\text{DRH20}} = \frac{2 * 0.13^2}{\lambda} = 0.45\text{m} \tag{60}$$

$$d_{f\,\text{polarizers}} = \frac{2 * 0.08^2}{\lambda} = 0.17\text{m}$$

The distance between the measuring antenna and the measured antenna is about 3 m, thus this distance is sufficient and the measurement will take place in the far field region.

The arrangement in the anechoic chamber shows Fig. 89 and the attachement to the rotating holder shows Fig. 90.
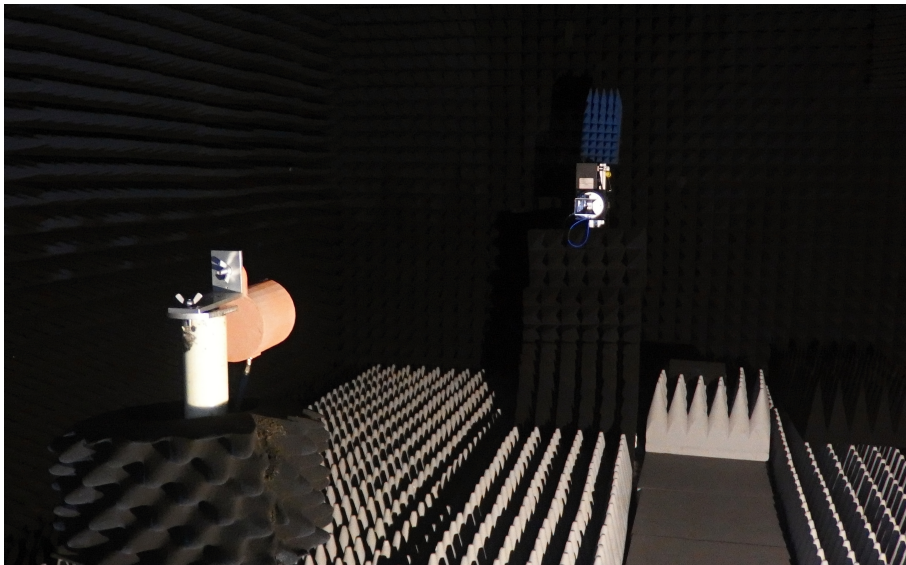


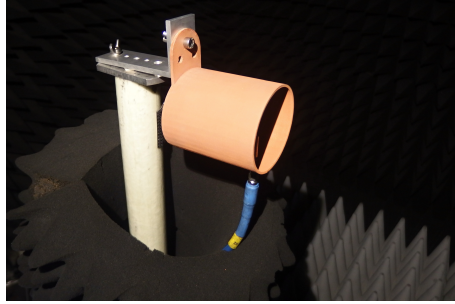Figure 89: The measurement arrangement in the anechoic chamber.

Figure 90: The attachment of the polarizers in the anechoic chamber.

## 12.1 Circular polarizer

In the Fig.91 and 92 reflection coefficients $S_{11}$ are showed. Because of not good impedance match and frequency shift of the polarizer with the aluminium spray metallizing, only the circular polarizer with copper spray metallizing will be used for next measuring.
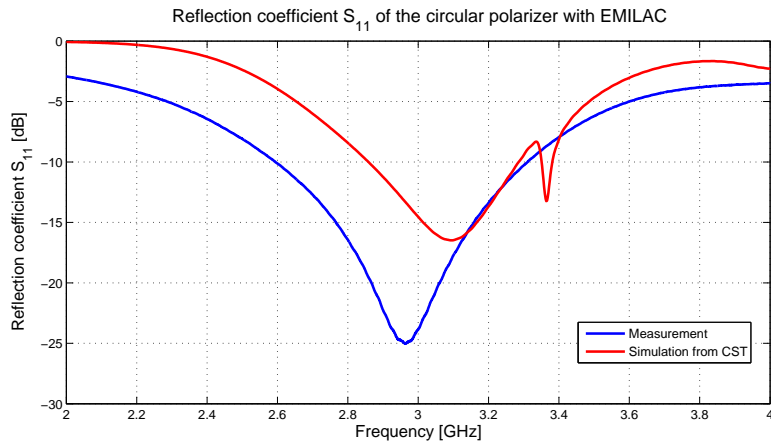


Figure 91: The reflection coefficient of the circular polarizer metallized with copper spray.
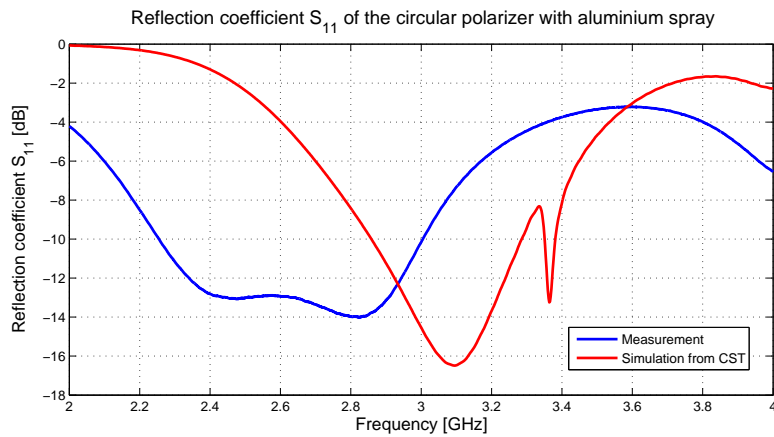


Figure 92: The reflection coefficient of the circular polarizer metallized with aluminium spray.

Measured and simulated radiation patterns of the circular polarizer with copper coating show Fig.93 and 94.
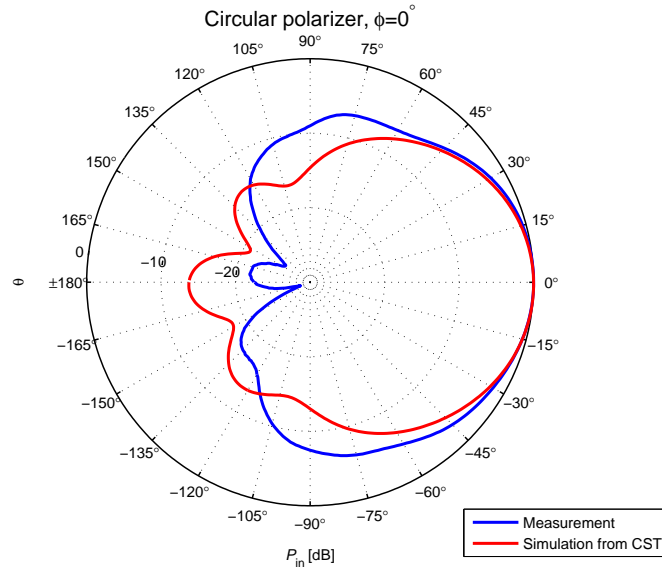


Figure 93: Radiation pattern of the circular waveguide in the $\phi = 0°$ plane.
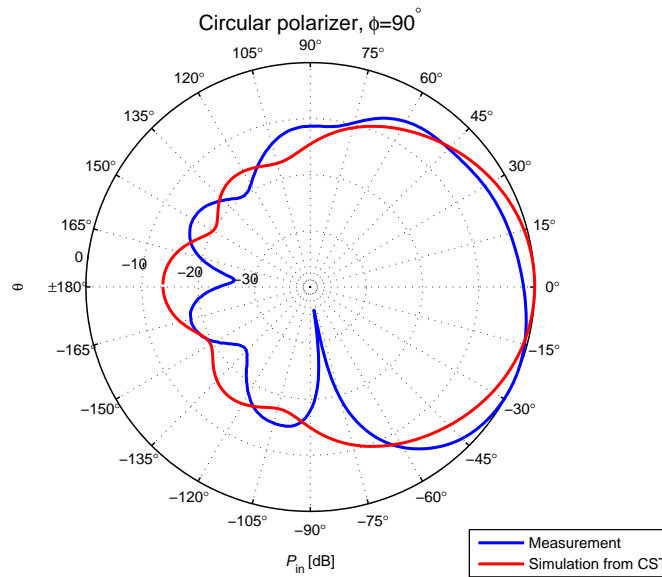


Figure 94: Radiation pattern of the circular waveguide in the $\phi = 90°$ plane.

The differences between simulated and measured values could be caused by not ideal holder, which can reflect some waves, not perfectly aligned antennas or with manufacturing errors. The copper spray coating could also be inhomogeneous and the current flow can influence the radiation patterns.

The polarization patterns were measured for $\theta$= -45, -30, -15, 0, 15, 30 and 45 ° and the corresponding patterns are shown in Fig. 95.



Figure 95: Measured polarization patterns of the circular polarizer.

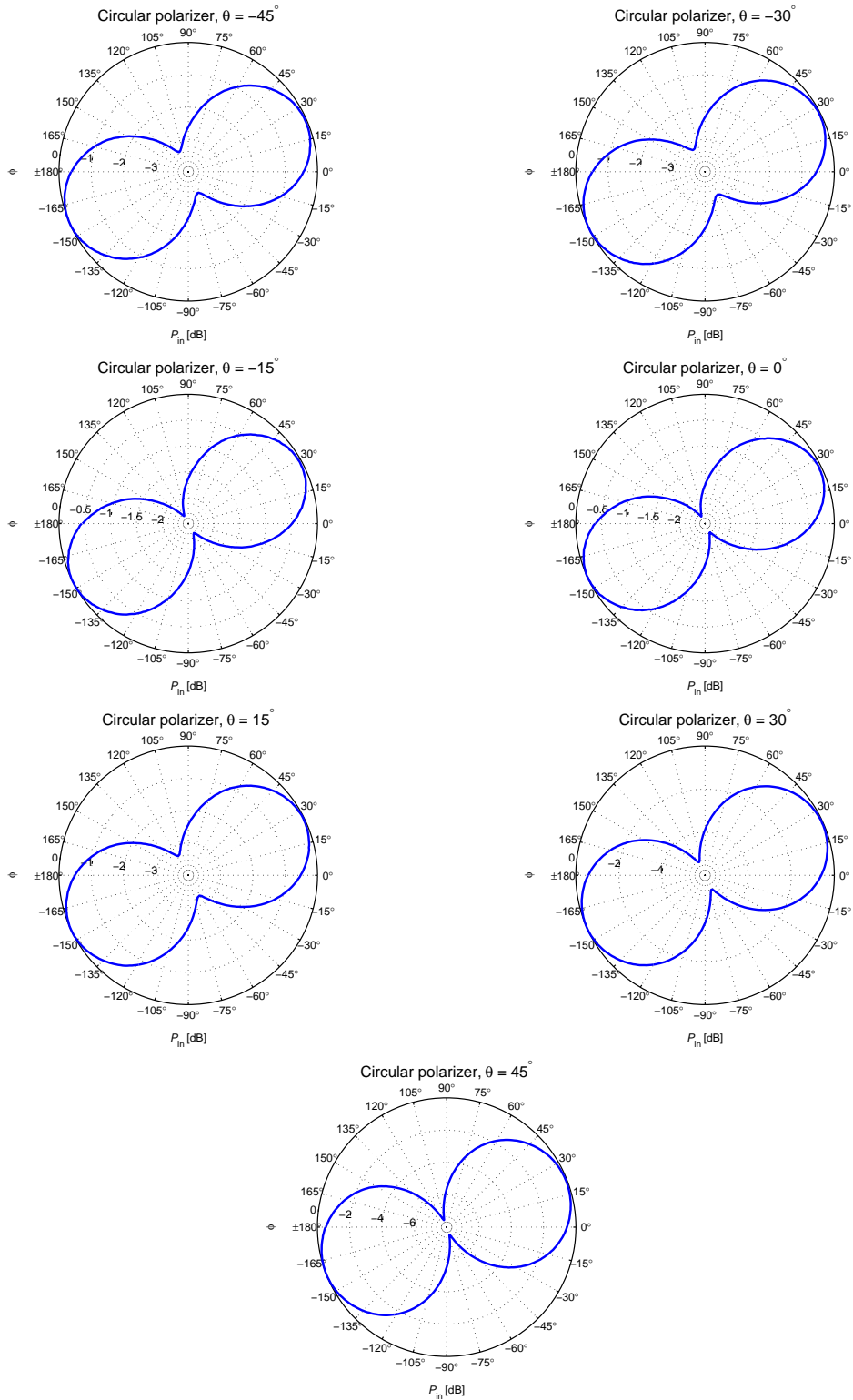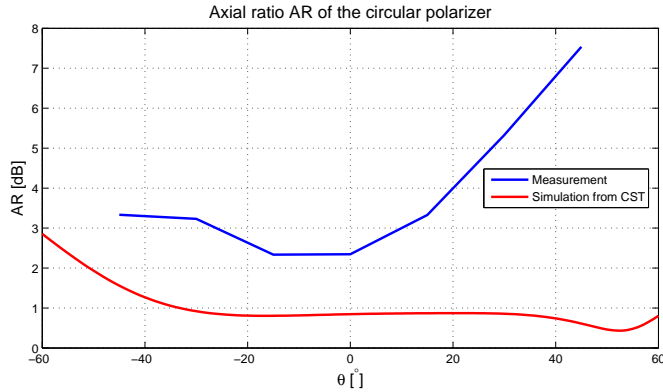Figure 96: Angle dependency of the axial ratio of the circular polarizer.

The gain of the antenna was measured using the measurement method with a reference antenna described in Section 4.1. As the transmission antenna and the reference antenna two DRH20 were used. Since DRH20 antenna is linearly polarized, the 3 dB polarization losses, as described in Section 3.2.1, occur and they need to be taken into account. The DRH20 gain is $G_r$= 9 dBi and the received power by the reference antenna $P_{r1}$=-48.7 dB, while the received power by the measured antenna was $P_{r2}$=-56.5 dB, thus the measured antenna gain $G_x$ is

$$G_x = P_{r2} - P_{r1} + G_r + L_{\mathrm{pol}} = -56.5 - (-48.7) + 9 + 3\mathrm{dBi} = 4.2\mathrm{dBi} \qquad (61)$$

Tab. 10 shows the overall comparison of the simulated values with the measured values of the circular polarizer with the copper spray metallizing. The plane $\phi = 0°$ is considered.

| Parameter | Simulation | Measurement |
|---|---|---|
| Gain | 8.3dBi | 4.2 dBi |
| $S_{11}$ | -14.5 dB | -24 dB |
| AR | 0.9 dB | 2.3 dB |
| HPBW | 69.9° | 79° |
| Sidelobe level | -13.2 dB | -21.8 dB |
| $BW_{-15\mathrm{dB}}$ | 5.1% | 13.1% |

Table 10: Overall comparison of the simulation and the measurement of the circular polarizer.

## 12.2 Elliptical polarizer

In the Fig.97 and 98 reflection coefficients $S_{11}$ are showed. Because of not good impedance match of the polarizer with the vacuum metallizing, only the elliptical polarizer with copper spray metallizing will be used for next measuring.
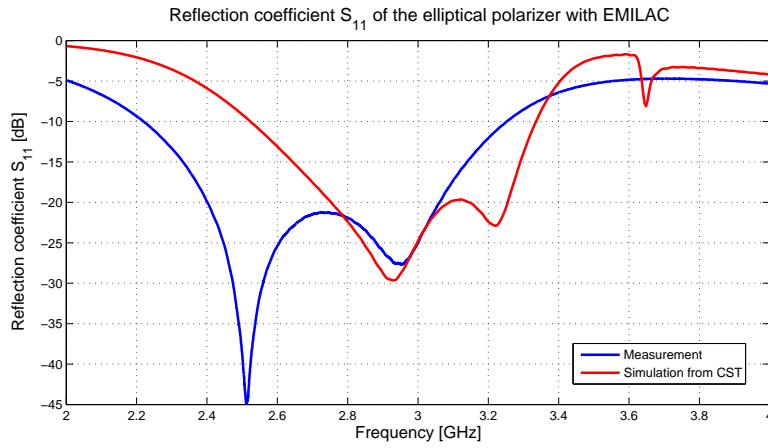


Figure 97: The reflection coefficient of the elliptical polarizer metallized with copper spray.
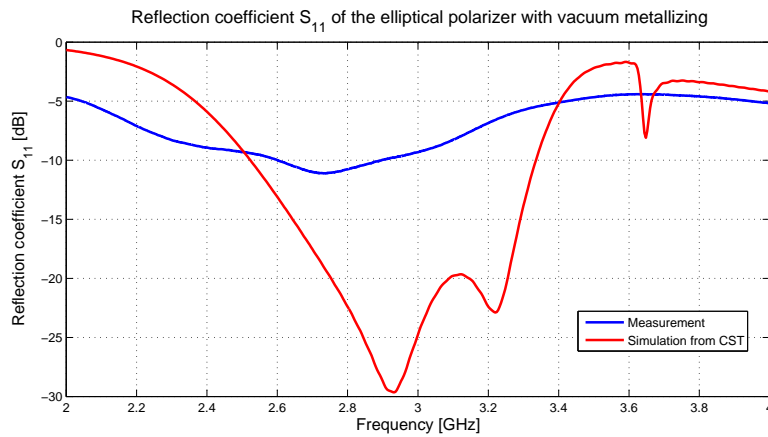


Figure 98: Reflection coefficient of the elliptical polarizer metallized with vacuum metallizing.

The measured and simulated radiation patterns of the elliptical polarizer with copper coating show Fig. 99 and 100.
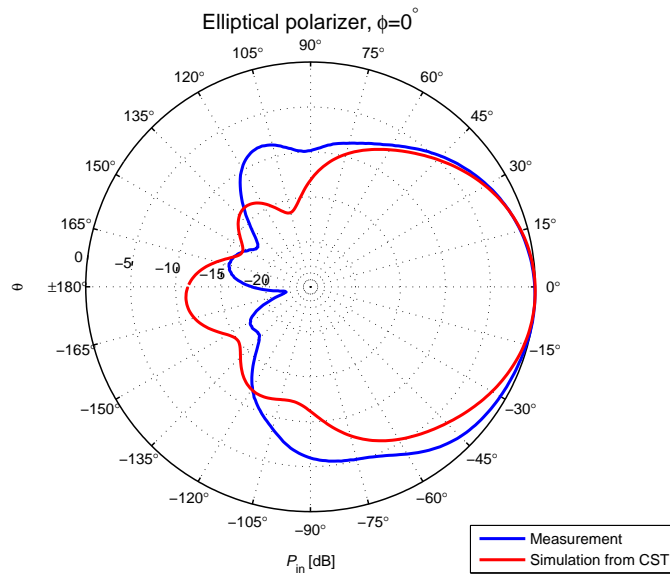


Figure 99: Radiation pattern of the elliptical polarizer in the $\phi = 0°$ plane.
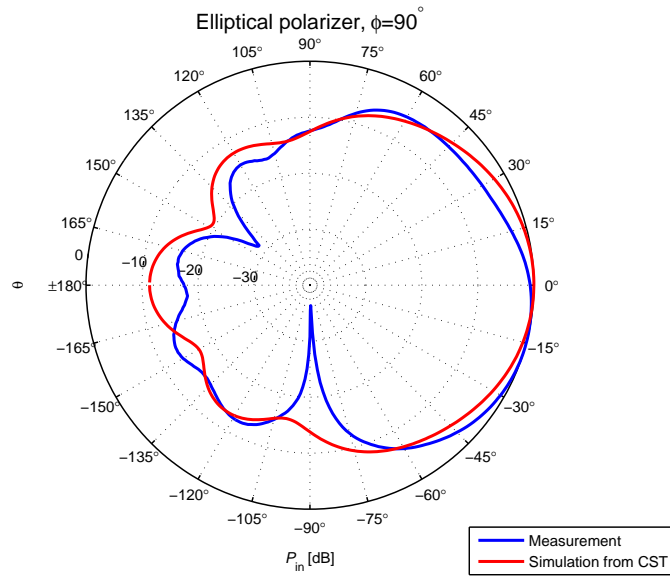


Figure 100: Radiation pattern of the elliptical polarizer in the $\phi = 90°$ plane.

The polarization patterns were measured for $\theta$= -45, -30, -15, 0, 15, 30 and 45 ° and the corresponding patterns are shown in Fig. 101. The shift can be cause with not perfectly aligned antennas or not exact dimensions like in the simulation. Also the connector attachment can influence the radiation and rotate the beam.
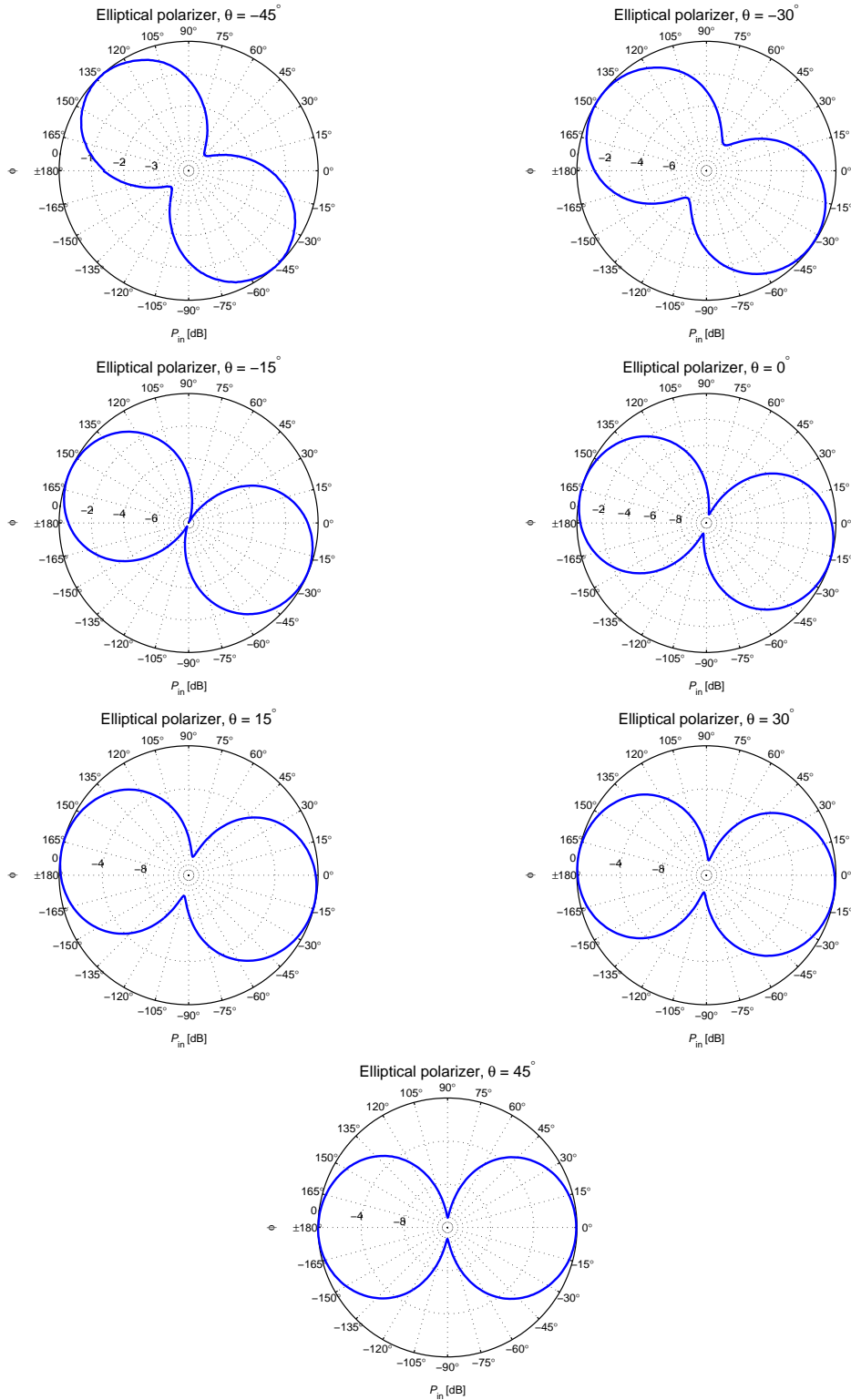


Figure 101: Measured polarization patterns of the elliptical polarizer.

Fig. 102 shows the big difference in the axial ratio of simulated and measured antenna, what could be caused by the rotation of the beam for above mentioned reasons.
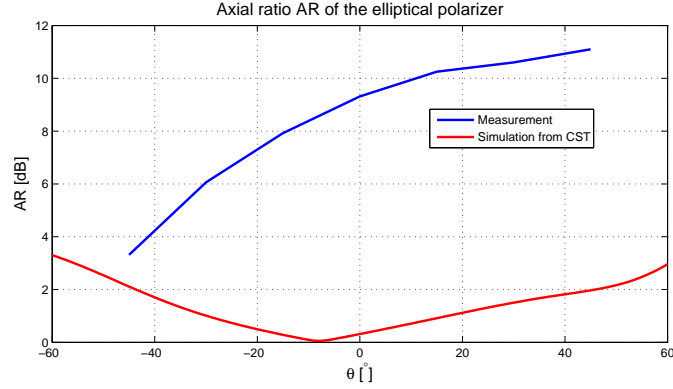


Figure 102: Angle dependency of the axial ratio of the elliptical polarizer.

The gain measurement is similar to the measurement of circular polarizer in Equation 61 and 3 dB polarization loss needs to be considered. The received power by the reference antenna $P_{r1}$=-48.7 dB, while the received power by the measured antenna was $P_{r2}$=-55 dB, thus the measured antenna gain $G_{\mathrm{x}}$ is

$$G_x = P_{r2} - P_{r1} + G_r + L_{\mathrm{pol}} = -55 - (-48.7) + 9 + 3\mathrm{dBi} = 5.7\mathrm{dBi} \qquad (62)$$

Tab. 11 shows the overall comparison of the simulated values with the measured values of the elliptical polarizer with the copper spray metallizing. The plane $\phi = 0°$ is considered.

| Parameter | Simulation | Measurement |
|---|---|---|
| Gain | 7.6 dBi | 5.7 dBi |
| $S_{11}$ | -24.6 dB | -25 dB |
| AR | 0.3 dB | 9.3 dB |
| HPBW | 74° | 92 ° |
| Sidelobe level | -11.1 dB | -8.5 dB |
| BW$_{-15\mathrm{dB}}$ | 27% | 22% |

Table 11: Overall comparison of the simulation and the measurement of the elliptical polarizer.

# 13  Conclusion

In this thesis a novel design of the polarizers were developed in the waveguide structure with perturbation elements. At the beginning basics on antenna, polarization, measurements and circular waveguides are described. In the next parts of this theses a polarizers and dual-mode horn theory and state of art is shown.

Two designs of polarizers were developed, the first polarizer in the circular waveguide with plates at opposite walls of the waveguide and the second polarizer in the elliptical waveguide section. The polarizers were designed and simulated in the CST Studio Suite. Because of the complexity of the analytical solution of these perturbed waveguides, a simulation and analysis of individual parameters were performed. After successful design, the polarizers were printed of ABS material using 3D printer. From each polarizer type two pieces were manufactured and metallized using different techniques. One piece was finished with a vacuum metallizing, one with a conductive aluminium spray and the last two with a highly conductive copper spray.

The measurements of the polarizers were performed in the anechoic chamber and the characteristics of the individual polarizers were tested. All polarizers were measured for their reflection coefficient. The polarizer with the vacuum metallized surface, which layer was too thin and the polarizer metallized with the aluminium spray, which matching was too low, were skipped and only the two polarizers with copper coating were used for next measurement, one of the circular shape and one of the elliptical shape.

The impedance matching of the circular polarizer showed a better matching (-24 dB) than the simulation (-14.5 dB). The measured reflection coefficient of the elliptical polarizer (-25 dB) corresponded very good to the simulation (-24.6 dB). The measured peak values of reflection coefficient were shifted to the lower frequencies, what can be caused by the inaccuracy of the printer or of the metallizing layer and so dimension mismatch between the model and printed part.

The axial ratios of developed polarizers were worse than the simulation. The measured AR of the circular polarizer 2.34 dB, compared to the 0.85 dB in the simulation, what is quite a good result for such structure and the polarizer works acceptable. For the elliptical polarizer an value 9.3 dB was measured, compared to the simulated 0.3 dB. In the lateral position the axial ratio was 3.3 dB and the antenna does not radiate directly in the $z$ direction.

The measured gains of the antennas indicates a differences in few dB. Namely, for the circular polarizer a simulation showed 8.3 dBi and measurement 4.2 dBi and the elliptical polarizer had simulated gain 7.6 dBi and measured 5.7 dBi

The horn for dual-mode excitation was not printed because of the big dimensions, the optimal length of the horn was designed to 305 mm.

The measurement could be influenced with more factors. The holder of the antenna used for measuring in the chamber, was not right designed and the measured antennas were not perfectly aligned and the holder extend too much and could case unwanted reflections. Also the connector assembly was not perfectly ideally attached and could influence the radiation patterns and other characteristics.

The next improvements of these polarizers could be done in the better attachment for the measurement and the antennas should be metallized with better technique, for example

with electroplating, what needed to make the surface of the antenna conductive, what could be possible with graphite layer. For 3D print conductive filaments could be used, which allowed electroplating too.

The developed antennas showed a good results with the arrangement in the waveguide section and also with the 3D printing technique. 3D print would be suitable for another antenna types too, because of an absence of any demanding manufacturing process like forming, cutting or other tooling. The only demanding process of the manufacturing is the metallizing of the surface, but the easy method with an conductive copper spray showed a good results.

This thesis verified, that 3D printing can be a very convenient manufacturing method for antenna development. The metallizing with the conductive copper spray showed a usable method with good results, while the other metallized technique had not good results.

# References

[1] Bertin, G.; Piovano, B.; Accatino, L.; Mongiardo, M., *Analysis and design of circular waveguide polarizers with elliptical Irises*. 30th European Microwave Conference, 2000.

[2] Simmons, A. J., *Phase shift by periodic loading of waveguide and its application to broad-band circular polarization*. IRE Transactions MTT, Dec. 1955.

[3] Lee, K. J.; Woo, D. J.; Lee, T. K.; Lee, J. W., *Coaxial-to-waveguide adapter generating circularly polarised wave*. Electronics letters, Vol. 46, No. 26, Dec. 2010.

[4] Jung, Y. B., *Ka-band polariser structure and its antenna application* Electronics Letters, Vol. 45, No. 18, Aug. 2009.

[5] Gao, S.; Luo, Q.; Zhu, F., *Circularly polarized antennas*. Wiley, 2014.

[6] In *https://upload.wikimedia.org* [online], [cit. 2016-4-11]. Available at: https://upload.wikimedia.org/wikipedia/commons/c/cb/Faraday-effect.svg.

[7] David M. Pozar, *Microwave Engineering, 4th edition*. Wiley, 2011.

[8] Constantine A. Balanis, *Antenna Theory: Analysis and Design, 3rd edition*. Wiley, 2005.

[9] Richard C. Johnson, *Antenna Engineering Handbook, 3rd edition*. McGraw-Hill, 1993.

[10] Sophocles J. Orfanidis, *Electromagnetic Waves and Antennas*. Rutgers University, 2014.

[11] Stephen F. Adam, Hewlett Packard, *Microwave Theory and Applications, 2nd edition*. Prentice Hall, 1969.

[12] Galuščák R., Hazdra P., *Circular Polarization and Polarization Losses*. Available at: http://www.attplus.cz/hamradio/projekty/article/cppl_b.pdf [cit. 2016-4-30].

[13] Lee, C. S. Lee; Lee, S. W.; Chuang, S. L.; Chuang, *Plot of Modal Field Distribution in Rectangular and Circular Waveguides*. IEEE Transactions on Microwave Theory and Techniques, Vol. 33, No. 3, 1985.

[14] Yen-Lin Chen, Tzihong Chiueh, Hsiao-Feng TengLee, *A 77–118 GHz resonance-free septum polarizer*. The Astrophysical Journal Supplement Series, 2014 March.

[15] Shih-Wei Wang, Chih-Hung Chien, Chun-Long Wang, Ruey-Beei Wu, *A Circular Polarizer Designed With a Dielectric Septum Loading*. IEEE Transactions on Microwave Theory and Techniques, Vol. 52, No. 7, 2004.

[16] George Ploussios, *Waveguide Polarizer having Conductive and Dielectric Loading Slabs to Alter Polarization of Waves*. US Patent No. 4,523,160, 1985.

[17] B. Ladányi-Turóczy, *Design of a Superelliptic Waveguide Polarizer*. 16th European Microwave Conference, 1986.

[18] Phillip D. Potter, *Dual Mode Horn Antenna*. US Patent No. 3,305,870, 1967.

[19] Phillip D. Potter, *A New Horn Antenna with Suppressed Sidelobes and Equal Beamwidths*. Technical Report No. 32-354, Jet Propulsion Laboratory, 1963.

[20] Herbert M. Pickett, John C. Hardy, Jam Farhoomand, *Characterization of Dual-Mode Horn for Submillimeter Wavelengths.* IEEE Transactions on Microwave Theory and Techniques, Vol. MTT-32, No. 8, 1984.

[21] Zobaer Ahmed, Asif Zaman, Lutfa Akter, *Parametric Analysis of Pickett Potter Horn Antenna.* IEEE International Conference on Telecommunications and Photonics (ICTP), 2015.

[22] Mohammad Asif Zaman, Md. Gaffar, Sajid Muhaimin Choudhury, M. A. Matin, *Optimization and Analysis of a Ka Band Pickett Potter Horn Antenna with Low Cross Polarization.* 6th International Conference on Electrical and Computer Engineering (ICECE), 2010.

[23] K. K. Agarwal, E. R. Nagelberg, *Phase Characteristics of a Circularly Symmetric Dual-Mode Transducer.* IEEE Transactions on Microwave Theory and Techniques, Vol. MTT-18, 1970.

[24] Chen Yao, Chen Ai-xin, Su Dong-lin *The Optimization Design of the Pickett Potter Horn Antenna for Ka Band.* Electromagnetic Compatibility and 19th International Zurich Symposium on Electromagnetic Compatibility, 2008.

[25] G. Yassin, S. Withington, P. Kittara, K. G. Isaak, *Theoretical Analysis of the Potter Horn Reflector Antenna for Submillimetre-wave Applications.* Tenth International Symposium on Space Terahertz Technology, Charlottensville, March 1999.

[26] Wade Paul, *Optimized Dual-mode Feedhorns.* [online], available at: http://www.w1ghz.org/antbook/conf/optimized_dualmode_feedhorns.pdf.

[27] Sergei P. Skobelev, Bon-Jun Ku, Alexander V. Shishlov, Do-Seob Ahn, *Optimum Geometry and Performance of a Dual-Mode Horn Modification.* IEEE Antennas and Propagation Magazine, Vol. 43, 2001.

[28] Mazánek, Hazdra, Polívka et al. *Lectures on "Antennas and EMC in Radiowave Communication" (A2M17AEK) and "Antenna Design and Technology" (A0M17NKA)*

[29] In *http://www.prusa3d.com/* [online], [cit. 2016-5-5], available at: http://www.prusa3d.com/wp-content/uploads/2015/09/black.jpg.

[30] In *https://www.matterhackers.com/3d-printer-filament-compare#standard-filament*, [cit. 2016-5-6].

[31] In *http://vacaero.com*, [online], [cit. 2016-5-10], available at: http://vacaero.com/information-resources/vacuum-pump-practice-with-howard-tring/1409-five-main-reasons-for-using-vacuum-part-5.html.

[32] In *http://www.itwcp.de*, [online], [cit. 2016-5-11], available at: http://www.itwcp.de/product-1241411-en.html?file=tl_files/downloads/cramolin/lacke/emilca-tech_sheet.pdf.

# Appendices

## Appendix A – RF Spin DRH20 Datasheet

# Double Ridged Waveguide Horn – Model DRH20

### Electrical Specifications

| | |
|---|---|
| Frequency Range | 1.7 GHz – 20 GHz |
| VSWR (max.) | < 1.5:1 |
| Impedance | 50 Ω |
| Connector | SMA female |
| RF Input Power | 20 W CW / 40 W Peak |

### Physical Specifications

| | |
|---|---|
| Width | 104 mm  (4.1 in) |
| Depth | 122 mm  (4.8 in) |
| Height | 78 mm  (3.1 in) |
| Weight | 290 g  (0.64 lb) |

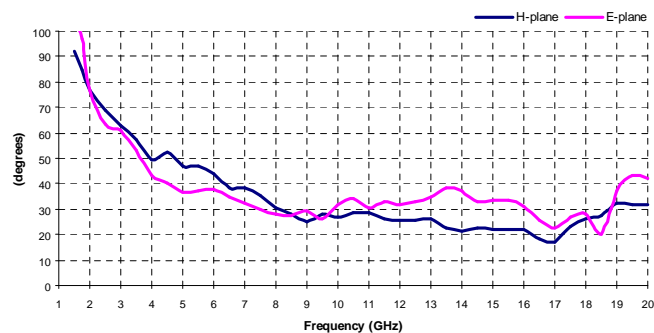- **Installed circular spirit level for easy setup**

### Typical Parameters

VSWR

Gain
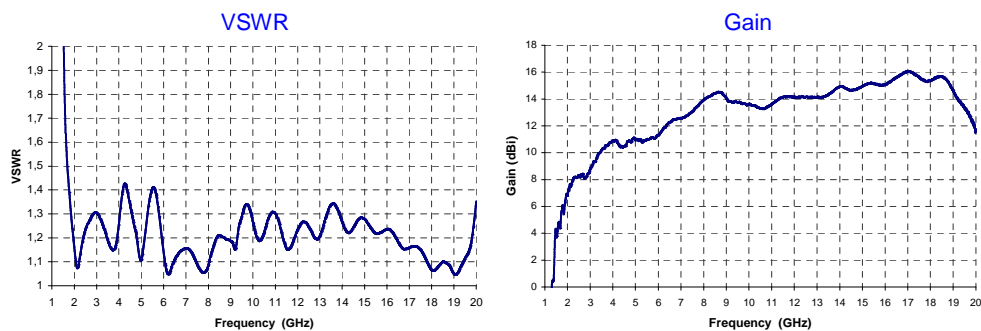
Half Power Beamwidth

# Appendix B – EMILAC spray datasheet

**CRAMOLIN®**

## CRAMOLIN® EMI Lacquer Art. No. 124

### Product description

EMI-LAC is a copper-based, silver-coated, highly conductive, protective coating which shields from electromagnetic waves. It ensures protection both from electromagnetic interferences (EMI) and from electromagnetic discharges (ESD). The subsequent shielding and attenuation can be achieved with thinner layers than with copper-based products normally used. EMI-LAC is easy to apply and exhibits high stability even under extreme environmental conditions such as heat and moisture. The lacquer is well-bonding and can be used without a primer on metal, glass and plastics. It does not attack the materials in common use and dries quickly.

### Application

Subsequent shielding of plastic cabinets from electromagnetic waves. Proves particularly effective in EDP, electronic laboratories, measurement technique, motorcar equipment and entertainment electronics. For the use in the manufacture of electrical contact connections and as protection against corrosion of manipulated aluminum casings. Best results will be obtained with film thicknesses between 40 μm and 75 μm.

### Please note

Surface to be treated has to be free of greases, oil, wax etc. Spray on the whole surface of parts to be treated, maintaining a distance of approximately 30 cm, otherwise the layer applied will flow. Should the spray nozzle get clogged, clean it using a thinner, acetone or turpentine.

### Technical Data

| | |
|---|---|
| Color: | copper |
| Pigment: | silver coated copper |
| Resin: | acrylic |
| Specific gravity (20° C): | 0,60 [g/cm3] |
| Drying conditions at | 10 min dry to touch |
| Room temperature: | 24 h totally cured |

Drying conditions in an oven:

10 min at room temperature
then ca. 30 min at 60 - 70° C in an oven

Surface resistance:

$<0,25\Omega$/square (50 μm film thickness)

Attenuation: 60 - 65 dB for 50 μm film thickness (ASTM ES 7-83)

| | |
|---|---|
| Necessary coat thickness: | 20 - 50 [μm] |
| Coverage: | 1 - 2 [m$^2$/can] (50μm Layer) |
| Temperature resistance: | -40 up to + 95 [° C] |

### Storage / Shelf Life

Shelf life is 2 years if stored correctly.
Package after emptying to be disposed via metal scrap.